Chapter 8

The Influence of Nonlinear Effects Upon Oscillation Regimes of Erbium-Doped Fiber Lasers

Y.O. Barmenkov and A.V. Kir'yanov

Additional information is available at the end of the chapter

http://dx.doi.org/10.5772/59146

1. Introduction

Erbium-doped fiber lasers (EDFLs) are contemporary sources of coherent radiation, attractive for numerous applications requiring both continuous-wave (CW) and pulsed operations, among which telecommunications in a wide wavelength range covering C and L bands ought to be emphasized. Pulsed operation, presenting big interest for practice, is attained in EDFLs by means of standard active and passive Q-switching and mode-locking techniques, capable of enforcing a laser to generate short pulses with durations ranged from hundreds fs to hundreds ns [1]. In the meantime, transients to CW lasing and a laser's relaxation frequency are also of close attention, e.g. when targeting the sensor applications [2, 3]. The detailed knowledge of the processes involved in Erbium-doped fibers (EDFs) to be used, when pumped, as a laser or amplifying medium in each of the referred regimes cannot be overestimated. The present work is a review of some of the most featuring nonlinear-optical effects that affect the oscillation regimes of EDFLs.

In spite of certain advantages (availability at the market, low cost, and easiness of handling), EDFLs demonstrate considerably lower efficiency as compared to the lasers based on Ytterbium-doped fibers. The basic cause is the multi-level energy scheme of Er^{3+} ions, which makes unavoidable absorption of photons at both the pump and laser wavelengths by the ions being at upper Er^{3+} levels, i.e. the "excited-state absorption" (ESA) [4, 5], including the state where 1.5-μm laser transition stems from. In other words, ESA presents a kind of "up-conversion" (UC) loss inherent to EDF; see section 2.

Another, nonlinear in nature, source of UC loss in EDFs and EDFLs on their base relates to so-called "collective" (concentration-related) effects arising in Er^{3+} ion pairs and in more complicate clusters (percentage of which grows with Er^{3+} concentration) [6]; see section 3. Appearance of the latter phenomenon is also associated with the multi-level energy scheme of Er^{3+} ions.

Eventually, the cases of low-and heavily-doped EDFs are to be carefully segregated and properly addressed if one looks for optimization of an EDFL.

One more kind of optical nonlinearity that arises in actively Q-switched (AQS) EDFLs is stimulated Brillouin scattering (SBS). Depending of the EDF length and Q-cell's modulation frequency EDFLs may operate in one of the two QS regimes: either in the "conventional" QS (CQS) one in which QS pulses are composed of several sub-pulses separated by a photon's round-trip time (with negligible pulse jitter) [7, 8], or in the essentially stochastic SBS-induced QS (SBS-QS) one where pulse amplitude is bigger by an order of value as compared with CQS but where pulses suffer severe jitter [9]. The results of an experimental study of the basins the CQS and SBS-QS regimes belong to and the basic spectral features of these regimes are discussed in section 4.

In section 5, the review's conclusions are formulated.

2. ESA in EDF at the pump and laser wavelengths

In this section, we report a study aiming at determination of the ESA's spectral dependence in EDF, covering the most important for applications spectral range, 1.48...1.59 μm, and at ~978 nm, the wavelength that usually is used for pumping EDFs by laser diodes (LDs). In the experiments discussed hereafter a low-doped silica EDF (*Thorlabs M5-970-125*, ~300 ppm of Er^{3+} concentration, Al-Ge-silicate host composition, *NA*=0.24, cut-off wavelength – 0.94 μm) was chosen to avoid possible effect of UC (observed in heavily-doped EDFs; see section 3). [This fiber belongs to M-series (fabricated through the modified chemical vapor deposition (MCVD) process), to be under scope in section 3 where Er^{3+} concentration effects are treated; "M5" signifies that small-signal absorption peaked at 978 nm is 5 dB/m.] The measurements were completed by modeling, a necessary chain in interpretation of the experimental results. The developed modeling also provides an estimate for the so-called ESA parameter, obtained at both pump and laser (signal) wavelengths, and thereafter allows determination of the EDF's net-gain coefficient, "deliberated" from the ESA interfere.

Figure 1 shows the fife level Er^{3+} ion energy scheme upon excitation at the pump (λ_p ≈980 nm) and signal (λ_s ≈1.5 μm) wavelengths, useful for the discussion presented in this section.

The equations that describe functioning of the Er^{3+} system, in accord to the scheme shown in Figure 1, at excitation at sole or at both excitation wavelengths (λ_s and/or λ_p) in the steady-state are written as follows:

$$\frac{\sigma_{12}I_s}{h\nu_s}N_1 - \frac{\sigma_{21}I_s}{h\nu_s}N_2 - \frac{\sigma_{24}I_s}{h\nu_s}N_2 - \frac{N_2}{\tau_{21}} + \frac{N_3}{\tau_{32}} = 0 \tag{1}$$

http://dx.doi.org/10.5772/59146

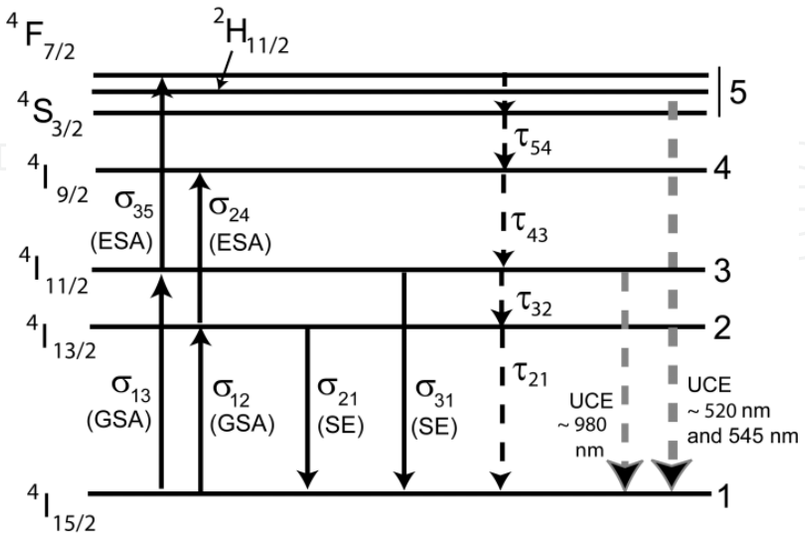

Figure 1. Fife-level scheme of Er^{3+} ion used in modeling. GSA and ESA indicate the ground-state and excited-state absorptions, UCE marks the up-conversion emission transitions (weak but detectable), σ_{ij} and τ_{ij} are, respectively, the cross-sections and decay times for the transitions between the levels i and j. Three closely-spaced energy levels $^4S_{3/2}$, $^2H_{11/2}$, and $^4F_{7/2}$ are regarded as an effective level "5".

$$\frac{\sigma_{13}I_p}{h\nu_p}N_1 - \frac{\sigma_{31}I_p}{h\nu_p}N_3 - \frac{N_3}{\tau_{32}} - \frac{\sigma_{35}I_p}{h\nu_p}N_3 + \frac{N_4}{\tau_{43}} = 0 \tag{2}$$

$$\frac{\sigma_{24}I_s}{h\nu_s}N_2 - \frac{N_4}{\tau_{43}} + \frac{N_5}{\tau_{54}} = 0 \tag{3}$$

$$\frac{\sigma_{35}I_p}{h\nu_p}N_3 - \frac{N_5}{\tau_{54}} = 0 \tag{4}$$

$$N_1 + N_2 + N_3 + N_4 + N_5 = N_0 \tag{5}$$

where N_0 is Er^{3+} concentration in the EDF core, N_i are the populations of the correspondent Er^{3+} levels (i=1 to 5), h is Plank constant, ν_p and ν_s are the frequencies of the pump and signal waves, and I_s and I_p are the pump and signal waves' intensities. The Er^{3+} parameters' values used in modeling are listed in Table 1.

Parameter	Value	Units
Low-signal absorption at 1531 nm (experimental data)	$\alpha_{s0} = 0.016$	cm^{-1}
Low-signal absorption at 977 nm (experimental data)	$\alpha_{p0} = 0.012$	cm^{-1}
Relaxation time for $^4I_{13/2} \rightarrow {}^4I_{15/2}$ transition [10]	$\tau_{21} = 10$	ms
Relaxation time for $^4I_{11/2} \rightarrow {}^4I_{13/2}$ transition[11]	$\tau_{32} = 5.2$	μs
Relaxation time for $^4I_{9/2} \rightarrow {}^4I_{11/2}$ transition [12]	$\tau_{43} = 5$	ns
Relaxation time for $(^4F_{7/2}/^2H_{11/2}/^4S_{3/2}) \rightarrow {}^4I_{9/2}$ transition [13]	$\tau_{54} = 1$	μs
Cross-section of $^4I_{15/2} \rightarrow {}^4I_{13/2}$ transition @ 1531 nm [14]	$\sigma_{12} = 5.1\times10^{-21}$	cm^2
Cross-section of $^4I_{15/2} \rightarrow {}^4I_{11/2}$ transition @ 977 nm [14]	$\sigma_{13} = 1.7\times10^{-21}$	cm^2

Table 1. EDF "M5" / Er^{3+} parameters used in modeling

2.1. Spectral features of ESA in low-doped EDF within the 1.48 to 1.59-μm range

The first experiment serves to reveal the existence of the ESA process in the EDF at pumping through $^4I_{15/2} \rightarrow {}^4I_{13/2}$ transition, refer to Figure 1. The UC emission (UCE) spectra were recorded in the wavelengths range near 980 nm ($^4I_{11/2} \rightarrow {}^4I_{15/2}$ transition). The pump source was a 12-mW narrow-line LD (*Anritsu Tunics Plus SC*), tunable through the spectral interval, λ_s=1.48...1.59 μm. Experimentally, light from the LD was launched into the EDF (length, 1 m) through a standard 980-nm / 1550-nm wavelength division multiplexer (WDM) while de-multiplexed backward emission from the EDF was registered by an optical spectrum analyzer (OSA, *Ando AQ6315A*). The recorded UCE spectra, at 10-mW in-fiber power and for four different excitation wavelengths λ_s, are shown in Figure 2(a). It is seen that UCE power depends on λ_s and that the maximal UCE signal spectrally matches the peak wavelength of the Er^{3+} ground-state absorption (GSA) contour. The appearance of the UCE spectra at λ_p ~980 nm is very similar to that of $^4I_{11/2} \rightarrow {}^4I_{15/2}$ emission, thus testifying for effective populating of Er^{3+} $^4I_{11/2}$ state at pumping the EDF at λ_s=1.48...1.59 μm and so for the presence of the ESA process ($^4I_{13/2} \rightarrow {}^4I_{9/2}$), followed by fast non-radiative ($^4I_{9/2} \rightarrow {}^4I_{11/2}$) relaxation. Note that no UCE spectral components in the range below 960 nm were detected.

The second experiment, allowing us to reveal the spectral dependence of ESA, was arranged through measurement of the integral lateral emission power collected from the EDF's lateral surface, using a Si photo-detector directly placed above the fiber. Given Si is sensitive from the visible to near-IR (Si band-gap wavelength is ~1.1 μm), the Si photo-detector (PD) does register the UCE signal (centered at ~980 nm) and does not the spontaneous emission (SE) from level $^4I_{13/2}$ (~1.5 μm); a scattered pump-light component was found to be extremely weak. The results obtained at various pump powers are shown in Figure 2(b) (see curves 1–3). For comparison, we also plot in this figure (by curve 4) the integrated backward UCE power measured using OSA (from a 10-cm EDF sample). It is seen that the spectral dependence of the UCE signal is similar to the one of ESA power on the excitation wavelength. In fact, the shape of the presented dependencies is established by a convolution of the known GSA and yet unknown ESA spectra of Er^{3+} (notice that the latter depends on Er^{3+} ions population inversion).

http://dx.doi.org/10.5772/59146

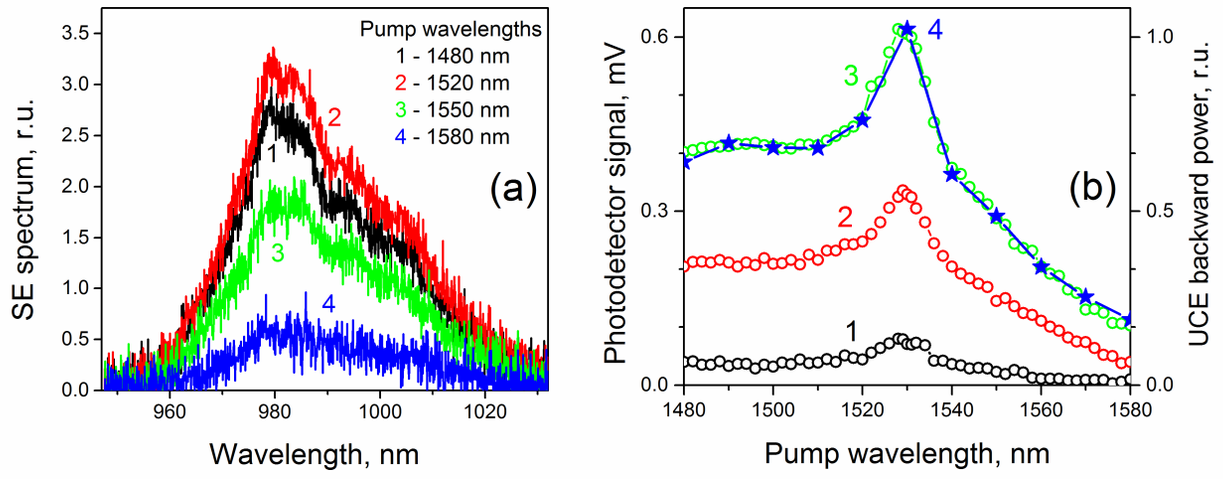

Figure 2. (a) UCE spectra at λ_s ~1.5-μm excitation. (b) Dependencies of PD signal (circles, left scale, curves 1 to 3) and normalized frontal UCE power (stars, right scale, curve 4) on excitation wavelength. Curves 1, 2, and 3 correspond to pump powers of 1, 5, and 10 mW; curve 4 is for 10-mW pump.

Considering the simplified Er^{3+} ion's model and the processes involved at excitation at λ_s ~1.5 μm (see Figure 1 and formulas (1-5)), we obtain simple formula for the normalized population of $^4I_{11/2}$ state, $n_3=N_3/N_0$ [11]:

$$n_3 = \frac{\varepsilon_s \gamma_s s_s^{\,2}}{1+\xi_s s_s + \varepsilon_s \gamma_s s_s^2}, \tag{6}$$

where $\varepsilon_s=\sigma_{24}/\sigma_{12}$ is the ESA parameter at signal wavelength, $\gamma_s=\tau_{42}/\tau_{21} \approx \tau_{32}/\tau_{21}$ (τ_{43} ≈5 ns is neglected in simulations given its smallness respectively the other decay times), $\xi_s=1+\sigma_{21}/\sigma_{12}$ is the spontaneous emission (SE) parameter at the signal wavelength, and $s_s=I_s/I_s^{sat}=P_s/P_s^{sat}$ is the saturation parameter for signal wave (with I_s being the signal wave intensity, $I_s^{sat}=h\nu_s/\sigma_{12}\tau_{21}$ the saturation intensity, $P_s=A_s I_s$, $P_s^{sat}=A_s I_s^{sat}$, P_s and P_s^{sat} the signal wave power and saturation power, respectively, and A_s the area of the Gaussian distribution of the signal wave in the EDF core). Notice that since $\varepsilon_s\gamma_s s_s << \xi_s$ ($\gamma_s \approx 7\times10^{-4}$ and $\varepsilon_s \le 0.6$, see below), the term with a second power on s in the denominator of (6) is omitted in further calculus. From formula (6), we find the normalized population n_3 averaged over the fiber core area if the pump wave intensity is taken to obey the Gaussian law, $s_s(r)=s_{s0}\exp[-2(r/w_s)^2]$:

$$\bar{n}_3 = \frac{1}{\pi a^2}\int_0^a n_3(r)\times 2\pi r dr = \frac{\varepsilon_s\gamma_s s_{s0}}{2\xi_s}\left(\frac{w_s}{a}\right)^2 \ln\left[\frac{1+\xi_s s_{s0}}{1+\xi_s s_{s0}\left(1-\Gamma_s\right)}\right], \tag{7}$$

where s_{s0} is the on-axis saturation parameter that depends on the pump power, P_s, as $P_s=I_s^{sat} s_{s0}(\pi w_s^2/2)$, a is the EDF core radius, w_s is the modal radius of the Gaussian wave, and Γ_s is the mode's to fiber core's radii overlap factor at λ_s. The parameter ξ_s comprises the ESA parameter ε_s, the measured EDF low-signal absorption coefficient $\alpha_{s0}=\Gamma_s\sigma_{12}N_0$, and the full-saturated fiber gain $g_s=\Gamma_s\sigma_{21}N_0-\Gamma_s\sigma_{24}N_0=g_{s0}-\varepsilon_s\alpha_{s0}$ (g_{s0} is the EDF net gain at λ_s):

$$\xi_s = 1+\frac{\sigma_{21}}{\sigma_{12}} = 1+\frac{g_{s0}}{\alpha_{s0}} = 1+\frac{g_s}{\alpha_{s0}}+\varepsilon_s. \tag{8}$$

Apparently, UCE power depends on n_3 that in turns depends on ε_s. It is worth wising that the latter can be easily found from the UCE lateral signal, registered using PD (see Figure 2(b)). The results of calculation of the ESA parameters are plotted in Figure 3(a) by filled symbols (left scale), where the ε_s-spectrum is normalized on the GSA peak value (at λ_s=1.531 μm). It is seen that the ESA parameter weakly depends on λ_s within the spectral interval 1.48 μm to 1.55 μm whilst it sharply grows as λ_s approaches ~1.6 μm; this behavior reminiscences the trend reported in [15].

The method to find the absolute values of the ESA parameter ε_s is based on the measurements of the EDF's transmission coefficient $T(\lambda_s, P_s)$, i.e. in function of excitation power, and subsequent comparison of the experimental dependencies with the simulated ones, obtained after integrating, through the fiber length, of the saturation parameter $s_{s0}(z)$, with the latter being obtained from the equation for the excitation wave propagating in the fiber (z is the direction of light propagation) (see [11]):

$$\frac{ds_{s0}}{dz} = -\alpha_{s0}\frac{\varepsilon_s}{\xi_s}\Gamma_s s_{s0} - \alpha_{s0}\frac{\xi_s-\varepsilon_s}{\xi_s^2}\ln\frac{1+\xi_s s_{s0}}{1+\xi_s s_{s0}\left(1-\Gamma_s\right)}. \tag{9}$$

Note that the contribution of amplified SE (ASE) to the output spectra was as low as 0.1–1.9% respectively to the overall transmitted power, provided a short (50 cm) EDF piece has been used.

The results of fitting of the experimental EDF transmission curves within the interval 1.48...1.59 μm are shown in Figure 3(a) by asterisks (see right scale). It is evident that these results, as the ones regarding the UCE experiments, almost coincide. The solid curve shown in this figure is the best fit of the experimental data by the polynomial regression.

The knowledge of the ε_s-spectrum for the 1.48...1.59 μm band allows one to find the spectral dependence of the net-gain coefficient g_{s0} in the EDF, which is the real gain in the fiber, in contrast to the gain coefficient g_s, the quantity commonly but uncritically dealt with in experiments and simulations with EDF and EDFL[13]: In fact g_{s0} is diminished by the ESA parameter's value. Figure 3(b) demonstrates the spectral dependences of the three coefficients (g_{s0}, g_s, and α_{s0}), where the spectra for g_s and α_{s0} were measured using standard methods (see

http://dx.doi.org/10.5772/59146

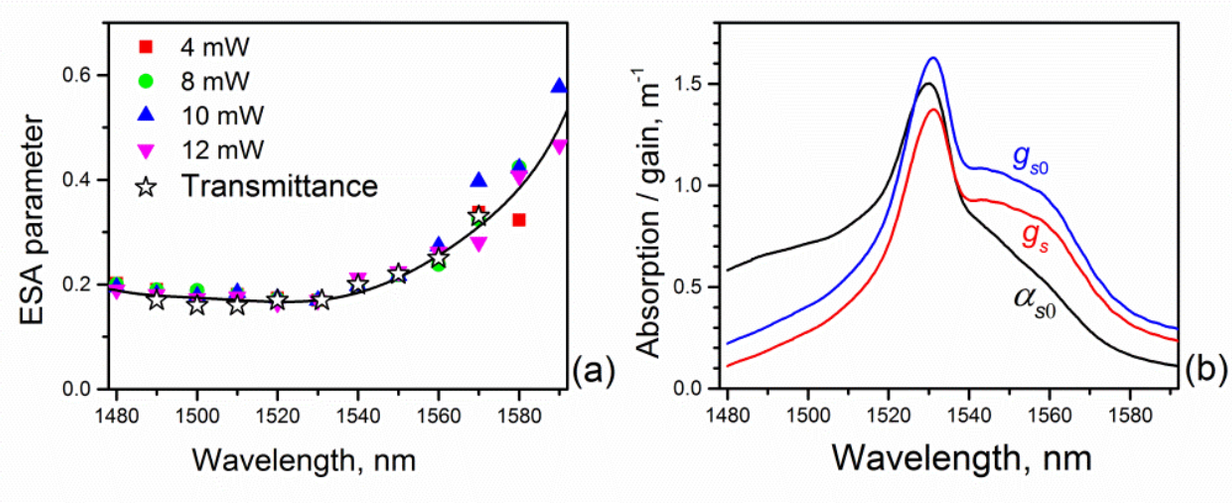

Figure 3. (a) ESA parameter ε_s calculated from the measurements of PD signal (filled symbols) and the ones of the EDF transmission coefficient (stars); solid line is the best polynomial fit. (b) Spectral dependencies of the EDF's small-signal absorption coefficient α_{s0}, full-saturated gain coefficient g_s, and net-gain coefficient g_{s0}.

e.g. Ref. 7) and the spectrum for g_{s0} was calculated using the g_s-and α_{s0}-spectra and the fitted ε_s-spectrum, taken from Figure 3(b). Worth noticing, the data obtained above are universal for any silica-based EDF weakly doped with Er^{3+}, where the "concentration" effects (to be discussed in section 3) are negligible.

2.2. ESA in low-doped EDF at 977 nm

We report here the results of a study of the other ESA process, $^4I_{11/2} \rightarrow {}^4F_{7/2}$ (see Figure 1), which takes the place when EDF is excited simultaneously at the two GSA wavelengths: λ_p ~977 nm (through $^4I_{15/2} \rightarrow {}^4I_{11/2}$ transition) and λ_s ~1531 nm (through $^4I_{15/2} \rightarrow {}^4I_{13/2}$ transition), a situation normally encountered in a diode-pumped (at λ_p~980 nm) EDFL or EDF-based amplifier (EDFA). Upon simultaneous excitation of EDF at these two wavelengths, population of $^4I_{11/2}$ state increases, resulting in significant growth of the pump-induced ESA loss (when $^4I_{11/2} \rightarrow {}^4F_{7/2}$ transition gets "switched on", see Figure 1). On the contrary, without the presence of a signal wave in the fiber, almost all ions will be at the upper laser level $^4I_{13/2}$, which leads to a lower absorption at λ_p.

The first experiment was focused on the demonstration of the presence of "pump-ESA", when EDF is pumped simultaneously at λ_p=977 nm and at λ_s=1531 nm. It was aimed to reveal of whether UCE is observed (through transitions $^2H_{11/2} \rightarrow {}^4I_{15/2}$ and $^4S_{3/2} \rightarrow {}^4I_{15/2}$ "5" → "3", see Figure 1), as following the ESA process at λ_p. Experimentally, an EDF piece was pumped, using 980 nm / 1550 nm WDM supporting up to 1 W of optical power, by the pump and signal beams from the same EDF's side. These beams were delivered from a standard fibered LD (λ_p=977 nm) and from another semiconductor laser with wavelength λ_s=1531 nm, followed by an EDFA. Figure 4 presents two photographs of lateral emission from the EDF sample when the fiber was pumped, respectively, (*i*) solely at wavelength λ_p (Figure 4(a)) and (*ii*) simultaneously at wavelengths λ_p and λ_s (Figure 4(b)); the incidence pump and signal powers were P_p=P_s=260

mW. One can readily see bright UCE (in the green spectral range, ~520–560 nm) when the EDF is pumped at both the wavelengths, and very weak UCE when it is pumped at λ_p only.

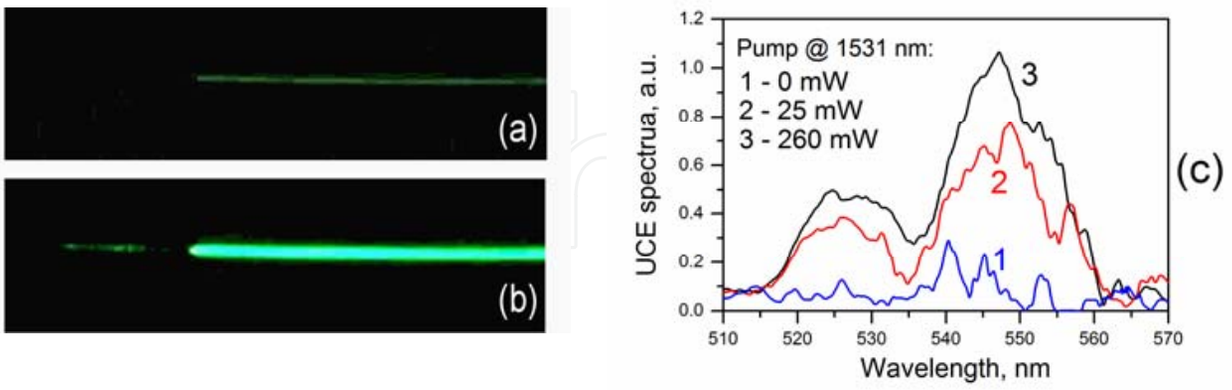

Figure 4. (a) and (b) Photographs of ~520/~545 nm UCE obtained from the EDF's surface at in-core excitation (a) only at λ_p=977 nm and (b) simultaneously at λ_p=977 nm and λ_s=1531 nm. (c) Frontal UCE spectra recorded from a 5-cm EDF sample at in-core excitation at pump wavelength (P_p=260 mW) and variable signal powers (P_s=0,25, and 260 mW).

The UCE spectra, obtained using a 5-cm EDF sample, are shown in Figure 4(c). The spectra were recorded for three signal powers (0, 25, and 260 mW) while fixed pump power (260 mW). One can see from the figure that even low-power (25 mW) signal radiation tremendously enhances UCE (compare curves 1 and 2) and that at further increasing signal power, up to P_s=260 mW, growth of the UCE power becomes slower, demonstrating a saturating behavior (compare curves 2 and 3). Thus, the signal at 1531 nm "ignites" the ESA process at λ_p and thereby increases the number of Er^{3+} ions in the ground state, resulting in an increase of the pump-light absorption. Consequently, there will be a non-negligible population of Er^{3+} ions on $^4I_{11/2}$ level and, as the fact of matter, a more effective ESA process at the pump wavelength, seen as growth of pump-induced loss.

Figure 5 shows the dependence of "green" UCE signal (transition "5"→"3", see Figure 1), detected from the EDF, on powers of pump and signal radiations launched into the fiber (in this case, again, the pump power was kept fixed, P_p=260 mW, and the signal power was varied, P_s=0...290 mW). Experimentally, lateral UCE power $P_{UCE}(P_s)$ was measured using a photomultiplier with a cesium cathode from a short section (~1 mm) of the EDF near its splice with WDM. It is seen that the UCE's behavior demonstrates the already noticed aspects: At very low signal power UCE is extremely weak, whilst upon its increase UCE first strongly enhances and then gets saturated.

Since UCE power is proportional to population of the 5th level of Er^{3+} ions, the experimental data can be fitted well by a simulated curve of normalized population inversion $n_5=N_5/N_0$ (N_5 is the population of the 5th Er^{3+} ion's level) averaged over the fiber core area, which confirms the theory we built. Considering that both the excitation waves (at 977 nm and at 1531 nm) have Gaussian spatial distributions, one can obtain from the steady-state rate equations for the Er^{3+} ion (formulas 1-5) the following expression for the averaged population $\bar{n}_5$:

http://dx.doi.org/10.5772/59146

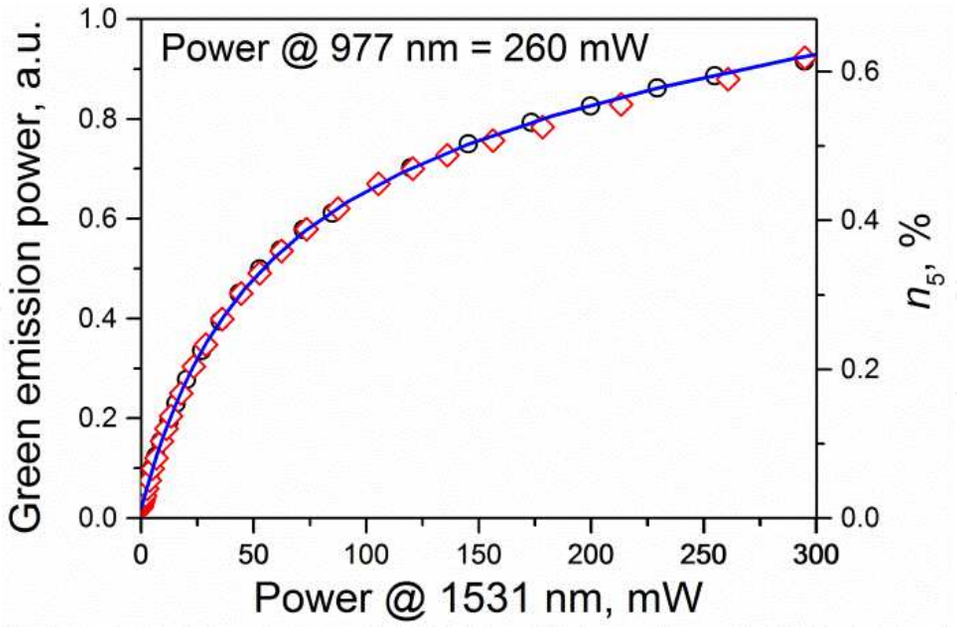

Figure 5. Dependence of UCE power on signal power (left scale): Circles and rhombs correspond to two different experimental series; plain curve is a theoretical fit of normalized inversion of the 5th Er^{3+} level (right scale).

$$\bar{n}_5 = \frac{\varepsilon_p \gamma_2}{a^2} \int_0^a \frac{1 - n_1(r) - n_2(r)}{1 + \varepsilon_p \gamma_2 s_p(r)} s_p(r) 2rdr \tag{10}$$

where the normalized populations $n_1(r)$ and $n_2(r)$ are taken from [16] (found from the same set of rate equations for the Er^{3+} ion); $\varepsilon_p = \sigma_{35}/\sigma_{13}$ is the ESA parameter at λ_p, $\gamma_p = \tau_{53}/\tau_{31}$ (with $\tau_{53} \approx \tau_{54} \approx 1$ μs and $\tau_{31} \approx \tau_{21} \approx 10$ ms, see Table 1), and $s_p = I_p / I_p^{sat}$ is the saturation parameter at the pump wavelength (I_p is the pump intensity, $I_p^{sat} = h\nu_p/\sigma_{13}\tau_{21}$, and $h\nu_p$ is the quanta energy at λ_p). As seen from Figure 5, the simulated curve for population of the 5th level ($\bar{n}_5$) fits well the experimental data, thus confirming correctness of the theory.

We found that the best way to find the ESA parameter at the pump wavelength, λ_p=977 nm, is to measure the EDF's nonlinear transmission coefficient at the pump wavelength in function of signal power, $T_p(P_s)$, and then compare this data with the simulated ones, obtained from the steady-state rate equations (formulas 1-5) for the fife level Er^{3+} energy diagram (see Figure 1). Considering the Gaussian radial intensity distributions for the pump and signal waves, the equations describing $T_p(P_s)$ at fixed pump power (P_p=260 mW in our case) take the form [16]:

$$\frac{dP_p(z)}{dz} = -\frac{4\alpha_{p0}}{\Gamma_p w_p^2}\left[\int_0^a [n_1(r,\ z) - (\xi_p - \varepsilon_p) n_3(r,\ z)] exp\left[-2\left(\frac{r}{w_p}\right)^2\right] rdr + \alpha_{BG}\right] P_p(z) \tag{11}$$

$$\frac{dP_s(z)}{dz} = \frac{4\alpha_{s0}}{\Gamma_s w_s^2}\left[\int_0^a [(\xi_s - \varepsilon_s) n_2(r,\ z) - n_1(r,\ z)] exp\left[-2\left(\frac{r}{w_s}\right)^2\right] rdr - \alpha_{BG}\right] P_s(z) \tag{12}$$

where α_{p0} is the small-signal EDF absorption and Γ_p is the pump wave to fiber core overlap factor, both at the pump wavelength, α_{BG} is the small background EDF loss (~3 dB/km for the EDF used), w_p is the radius of the Gaussian distribution of pump wave, and $\xi_p=1+\sigma_{31}/\sigma_{13}$ is the SE parameter at the pump wavelength. The normalized populations of Er^{3+} levels n_1, n_2, and n_3 are found from the rate equations for the Er^{3+} ion (the routine is not discussed here because of its completeness; refer for details to [16]).

Actually, the coefficient adjacent to P_p from the left side (Equation (11)) is the EDF absorption coefficient at the pump wavelength, whereas the one adjacent to P_s from the left side (Equation (12)) is the EDF gain at the signal wavelength; both the coefficients depend on the pump and the signal powers. It is worth of mentioning that the set of equations (11) and (12), added by the corresponding boundary conditions, can be also used for modeling a CW EDFL.

Figure 6 shows the EDF transmissions measured for three different EDF lengths along with the best fits obtained using equations (7) at varying ε_p and ξ_p (and as the result their most relevant values found to be: ε_s=0.17 and ξ_s=1.08, both at 1531 nm). As seen from the figure, the best fitting of the experimental EDF transmission at the pump wavelength is provided at ε_p=0.95 and ξ_p=1.08. Thus, the ESA cross-section at the pump wavelength is strong enough (being less than the GSA one only slightly), which ought to affect (decrease) an EDFL's efficiency via the pump-induced loss distributed along the active fiber.

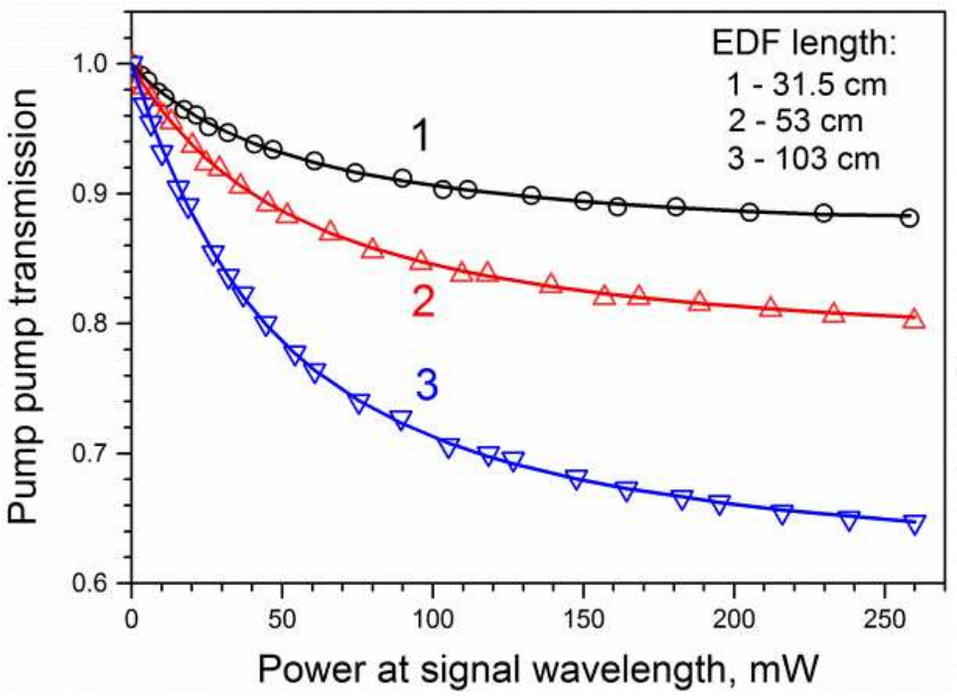

Figure 6. Experimental (symbols) and theoretical (curves) dependencies of pump (λ_p=977 nm) wave's transmission coefficient on signal (λ_s=1531 nm) wave's power; the data are obtained for three different EDF lengths (indicated in the inset). Theoretical curves are the best fits to the experimental data obtained at ε_p=0.95 and ξ_p=1.08.

http://dx.doi.org/10.5772/59146

2.3. Effect of ESA in EDF upon efficiency of CW EDFL.

We discuss hereafter the results of a theoretical study of influence of ESA inherent in Er^{3+} ions upon efficiency of an EDFL assembled in the linear (Fabry-Perot) configuration. The laser setup we shall deal with at modeling is shown in Figure 7. The low-doped EDF discussed above was considered to be an active medium and two fiber Bragg Gratings (FBGs) – to form selective couplers of the cavity, both centered at λ_s=1550 nm, the laser (signal) wavelength. The EDF length was chosen to be 4 m whereas the EDFL cavity length L_c, including the EDF piece and FBGs' tails, to be 6 m. Pump power on the EDF input was fixed in modeling at 200 mW.

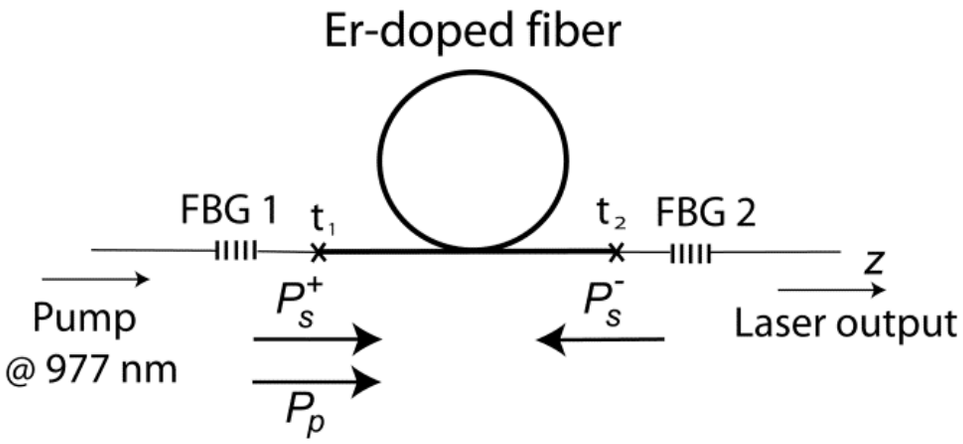

Figure 7. Sketch of the EDFL's geometry: $P_s^+$and P_s^- are the laser (signal) waves' powers propagating in the positive (+) and negative (-) z direction, respectively; P_p is the pump power propagating in the positive z direction; t_1 and t_2 are the transmissions on the fibers' splices.

We imply (see Figure 7) that the pump wave at 977 nm (absorption peak of $^4I_{15/2} \rightarrow {}^4I_{11/2}$ transition, see Figure 1) propagates rightward while the laser waves – rightward (marked by "+" superscript) and leftward (marked by "–" superscript), respectively. In the scheme, FBG1 plays the role of a rear 100% reflector (reflection R_1=1), transparent for the pump wave, whereas FBG2 forms an output coupler with reflection R_2 varied for optimizing the laser efficiency. To decrease loss on the fiber splices, both FBGs were considered to be written in a photosensitive fiber with waveguide parameters similar to the EDF's ones. At the laser wavelength the low-signal EDF absorption α_{s0} was taken to be 0.0069 cm^{-1}, according to [17].

The laser is simulated by applying the two contra-propagating laser waves' model discussed in details in [17] with taking into account Gaussian distributions of the laser and pump waves. In this model, the pump wave is described by equation (11) and the signal waves – by equation (12) with a small modification being that powers of the two contra-propagating signal waves are assumed to be governed by the equation:

$$\frac{dP_s^{\pm}(z)}{dz} = \pm \frac{4\alpha_{s0}}{\Gamma_s w_s^2}\left[\int_0^a [(\xi_s - \varepsilon_s)n_2(r,\ z) - n_1(r,\ z)]exp\left[-2\left(\frac{r}{w_s}\right)^2\right]rdr \mp \alpha_{BG}\right]P_s^{\pm}(z) \quad (13)$$

In equation (13) the superscripts "*s*" stand for the laser wavelength (1550 nm). The model includes also the two contra-propagating waves of SE (not shown in Figure 7) spectrally centered at λ_{se}=1531 nm (this wavelength corresponds to the GSA peak of $^4I_{15/2} \rightarrow {}^4I_{13/2}$ transition), powers of which obey the equation:

$$\frac{dP_{se}^{\pm}(z)}{dz} = \pm\left[g_{se}(z)P_{se}^{\pm}(z) \mp \frac{\Omega}{4\pi}\frac{\alpha_{se0}P_{se}^{sat}}{\Gamma_{se}}\int_0^a n_2(r,\ z)2rdr\right] \tag{14}$$

where the second term on the right side is the SE power generated by a short fiber section *dz*, α_{se0}=0.016 cm^{-1} is the low-signal absorption at λ_{se}, P_{se}^{sat} is the saturation power at 1531 nm, Γ_{se} is the overlap factor for the SE waves, $\Omega=\pi NA/n^2$ is the fraction of SE photons guided by the EDF core in each direction, and n is the modal refractive index at λ_{se}. The EDF gain at λ_{se} is written as

$$g_{se}\left(z\right) = \frac{4\alpha_{se0}}{\Gamma_{se}w_{se}^2}\left[\int_0^a\left[\left(\xi_{se} - \varepsilon_{se}\right)n_2(r,\ z) - n_1(r,\ z)\right]exp\left[-2\left(\frac{r}{w_{se}}\right)^2\right]rdr - \alpha_{BG}\right] \tag{15}$$

The boundary conditions are written as:

$$P_p(z=0,\ t) = P_{p0} \tag{16}$$

$$P_s^{+}(z=0,\ t) = P_s^{-}(z=0,\ t)R_1t_1^2 \tag{17}$$

$$P_s^{-}\left(z=L_c,\ t\right) = P_s^{+}\left(z=L_c,\ t\right)R_2t_2^2 \tag{18}$$

$$P_{se}^{+}(z=0,\ t) = P_{se}^{-}\left(z=L_c,\ t\right) = 0 \tag{19}$$

$$P_s^{out}(t) = P_s^{+}\left(z=L_c,\ t\right)\left(1 - R_2\right)t_2 = 0 \tag{20}$$

where P_{p0} is the pump power at the EDF input and P_s^{out} is the EDFL output power. To simplify calculations, we considered that t_1=t_2=0 (i.e. no loss on the fiber splices).

The EDFL's efficiency as a function of FBG2's reflectivity R_2, simulated using the laser model described above, is depicted in Figure 8(a). The EDFL was modeled for four different "versions" of the energy level system: Without considering all the ESA transitions (curve 1); with considering the pump ESA only (curve 2) and the signal ESA only (curve 3); with considering all the ESA transitions (curve 4).

The first important observation is that the optimal reflection of output FBG2, at which EDFL demonstrates the maximal efficiency, is drastically decreased when the ESA transitions are accounted for. For instance, the optimal reflection of FBG2 is ≈66% when only the EDF background loss (3.1 dB/km, see Table 1) is present (curve 1), whereas it is ≈11% when all kinds

http://dx.doi.org/10.5772/59146

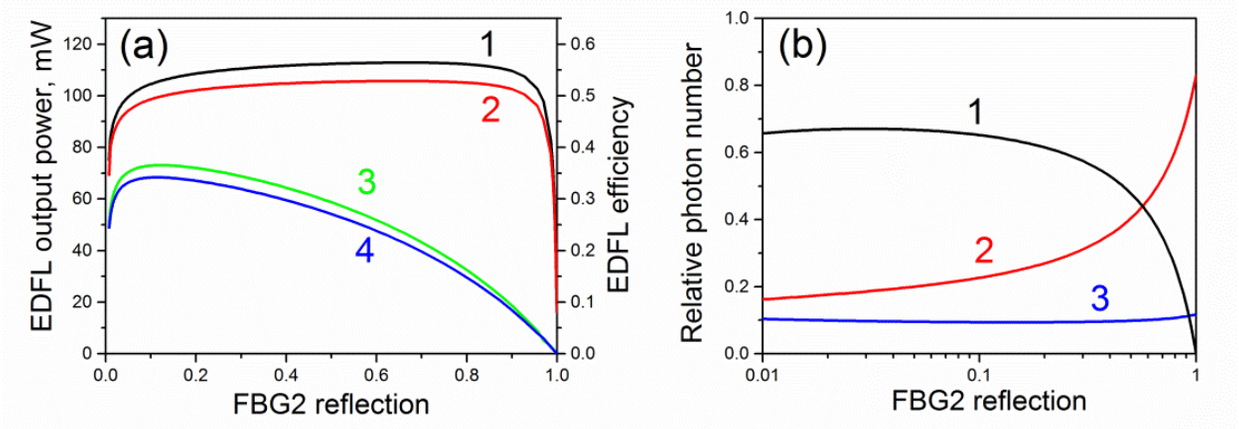

Figure 8. (a) EDFL output power and (b) fractions of the absorbed pump photons spent on the laser output (quantum efficiency) as functions of output (FBG2) reflectivity, R_2. The designations of curves 1 to 4 are given in the text. The small fraction of pump photons spent at the background loss and the ASE contribution are not shown.

of the ESA loss are accounted for (curve 4). The other important fact is that the range of FBG2's reflections, in which the output laser power varies within 10% (with respect to its maximum value if all the ESA transitions are considered), is relatively broad: ~2.5% to ~34%. At the optimal FBG2's reflectivity (R_2=11%) the laser efficiency reaches ~34% (implying all fiber splices are made lossless).

The fractions of pump and signal photons spent on the ESA transitions with respect to the absorbed by EDF pump photons are shown in Figure 8(b). It is seen that the contribution of the signal ESA loss is bigger when FBG2's reflection is bigger (curve 2). Furthermore, if reflection of the output coupler approaches 100%, the absorbed pump power is spent entirely on the ESA transitions (see curves 2 and 3) and no photons at the laser output are produced (see curve 1). At optimal FBG2's reflectivity (≈11%), about 23% of absorbed pump photons are spent on ESA at the laser wavelength and about 9.5% on ESA at the pump wavelength. Note that the sum of the relative photon numbers, as can be revealed from curves 1, 2 and 3, is approximately equal to 1 in the whole range of FBG2's reflections.

The reader is advised here to refer to [18] for comparison of the developed theory with some of the experimental data on laser efficiency of EDFLs based on the EDF of M-type with relatively high Er^{3+} concentrations.

Finally, we conclude that the ESA processes at the laser and pump wavelengths strongly affect an EDFL's efficiency and output coupler's optimal reflectivity, at which the laser output power is maximal.

3. Er^{3+} concentration effects in EDF

In this part, we shall discuss the Er^{3+} concentration effects in EDFs resulting in a reduced efficiency of EDF based lasers and amplifiers, which is associated with the phenomenon of

Er^{3+} ions' clustering that leads, in turn, to non-saturable absorption (NSA) through inhomogeneous up-conversion (IUC).

For our experiments we selected the most representative commercial EDFs fabricated through the MCVD and direct nanoparticle deposition (DND) processes; all the fibers under scope in this section are similar in the sense of Er^{3+} doped core's chemical composition being the most common alumino-silicate glass (in the case of MCVD-EDFs with addition of germanium). The first series of the EDFs (MCVD-based, "M"-series) includes two fibers: M5-125-980 and M12-125-980 (*Fibercore*), hereafter M5 and M12, and the second series (DND-based, "L"-series) – three fibers: L20-4/125, L40-4/125, and L110-4/125 (*Leikki* / *nLight*), hereafter L20, L40 and L110. These fibers have very similar waveguide parameters and differ mainly in Er^{3+} doping level. [Notice that the EDFs employed in the whole of above experiments, see Section 2, belong to M-series.]

3.1. Absorption and fluorescence spectra

The EDFs' absorption spectra are shown in Figure 9(a) where Er^{3+} transitions $^4I_{15/2} \rightarrow {}^4I_{11/2}$ (within a 940...1020 nm range with a peak at 978 nm) and $^4I_{15/2} \rightarrow {}^4I_{13/2}$ (within a 1400...1600 nm range with a peak at 1.53 μm) are featured. The spectra were obtained using a white light source with fiber output and OSA with 1-nm resolution. It is seen that the absorption spectra of the EDFs of both series have a very similar shape (given by similarity of core glass chemical compositions), differing only in intensity. The ratio of the peaks' magnitudes at 1.53 μm and at 978 nm was measured to be equal to ~1.6, for the M and L EDFs.

Figure 9(b) demonstrates the normalized fluorescence spectra for L fibers (to simplify the picture the spectra for M fibers are not shown), measured at the maximal pump power at 978 nm, P_p ~400 mW, within the 450...1650 spectral range (the area nearby the pump wavelength is cut out). In this experiment the lateral geometry, when fluorescence is captured by a multimode fiber patch cord from the lateral surface of the short fiber samples, was arranged. In spite of Er^{3+} concentration increases in the row of fibers L20 → L40 → L110, the Er^{3+} fluorescence band, centered at ~1.53 μm, is indistinguishable in shape. Although the 1.53-μm band dominates in the EDFs' fluorescence spectra, there also exist the spectral lines at its anti-Stokes side (~450...1100 nm), which evidences the presence of UC. Note that, in contrast to the ~1.53-μm band's stability against Er^{3+} concentration, the higher Er^{3+} content, the more intense the UCE (compare curves 1 – 3 in Figure 9(b)).

To understand the origin of UCE and the dependence of UC intensity upon Er^{3+} concentration in the EDFs, let's refer to Figure 10 in which the scheme of Er^{3+} energy levels and a sketch of the processes involved at the excitation at λ_p=978 nm are presented. UCE (shown in the figure by grey arrows) seems to be mostly associated to Er^{3+} ion clusters being in states $^4I_{11/2}$ and $^4I_{13/2}$, because the ESA process, equally acting for single and clustered Er^{3+} ions, is ineffective at 978-nm excitation.

http://dx.doi.org/10.5772/59146

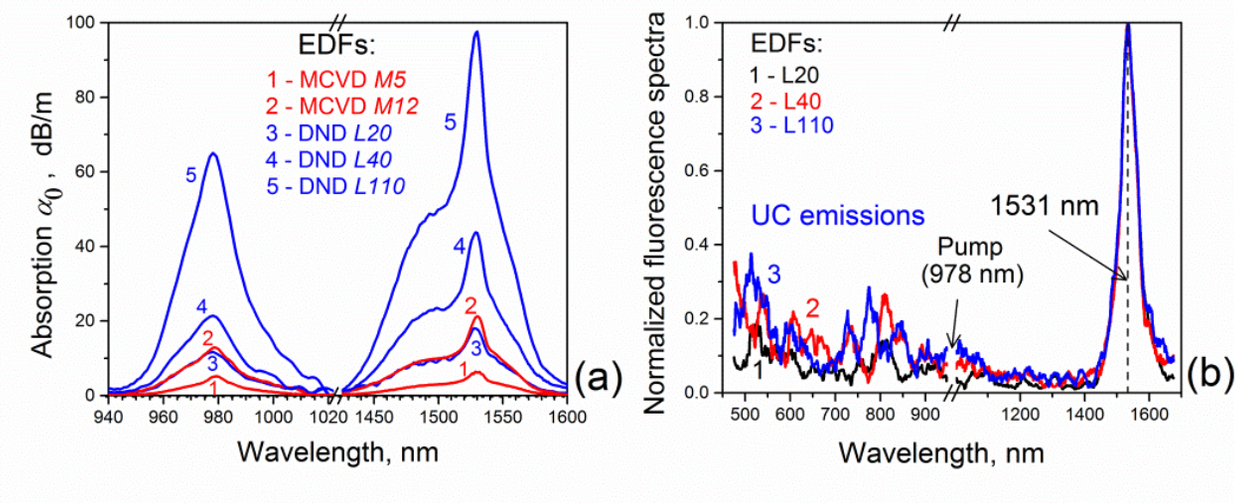

Figure 9. (a) Absorption spectra of the EDFs of L-(blue curves) and M-(red curves) series in the near-IR. (b) Fluorescence spectra of the EDFs of L-series in the VIS...near-IR spectral range at 978-nm pumping.

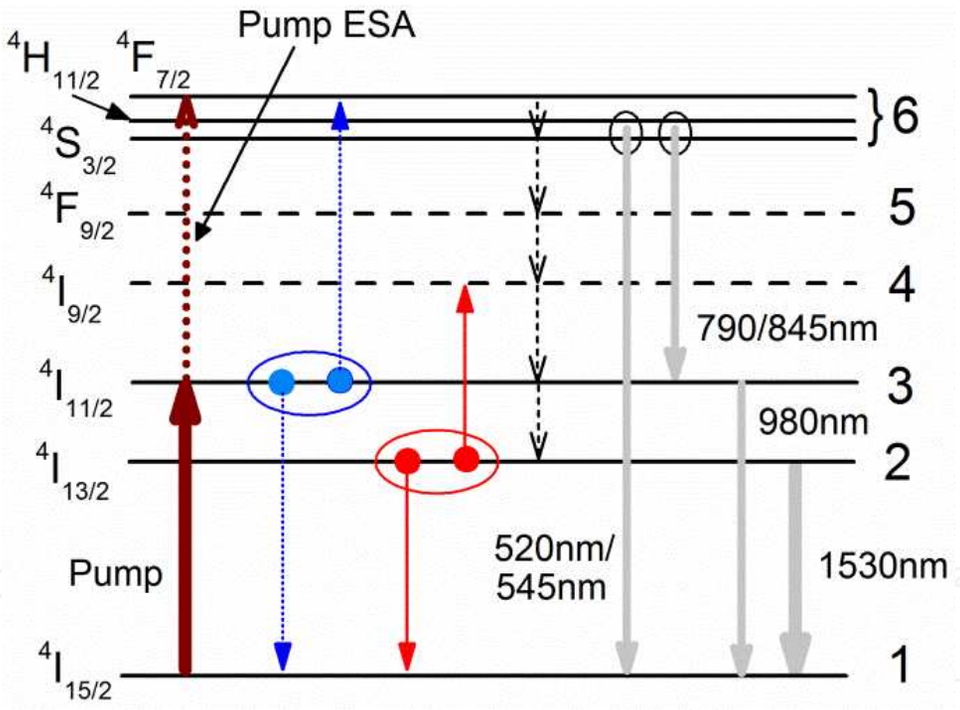

Figure 10. Scheme of Er^{3+} energy levels, applicable for the EDFs with high Erbium content. Functioning of Er^{3+} clusters (shown for simplicity as ion pairs) is sketched by the blue and red arrows for long-living manifolds $^4I_{11/2}$ and $^4I_{13/2}$; the black dotted arrows depict non-radiative relaxations; the grey arrows show the UC and "fundamental" (1.53-μm) emissions; the short-living levels are shown by dashed lines.

3.2. Fluorescence decay kinetics

Like at the fluorescence spectra' measurements discussed above, the kinetics of near-IR fluorescence at ~1.53 μm was detected using the lateral geometry. However, the pump light

at 978 nm was in this case switched on / off by applying a rectangular modulation of LD current at Hz-repetition rate. The launched into the EDF samples pump power was varied between zero and ~400 mW. The fluorescence signal was detected either using an InGaAs PD with a Si filter placed between the fiber and a multimode patch cord delivering fluorescence to PD (being so the measurements above ~1.1 μm where the use of Si filter allows cutting off the pump light's spectral component), or using a fast Si-PD with no spectral filtering applied (being in fact the measurements below ~1.1 μm), placed directly above a slit segregating a portion of fluorescence from the EDF's surface. To diminish ASE and re-absorption on the results, we used short (~0.5 cm) EDF pieces.

Typical kinetics of the fluorescence signal, recorded after switching pump light at 978 nm off, are presented in Figure 11 for the heavier doped EDFs M12 (a) and L110 (b); the data were acquired using InGaAs-PD with Si filtering (transmission band above 1.1 μm). We don't present here the results for other, lower doped, EDFs as these showed similar but less featured trends in the decay kinetics.

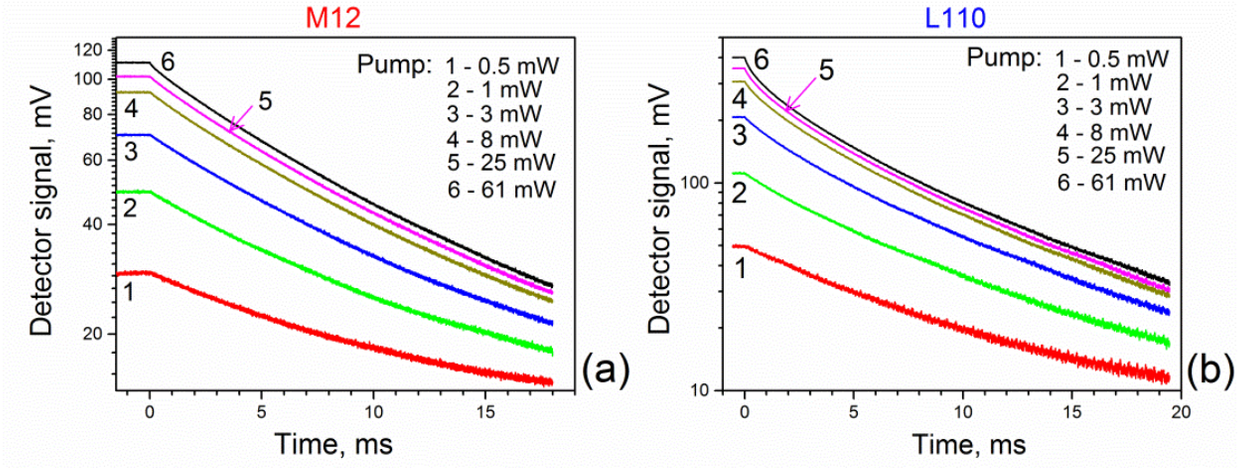

Figure 11. Fluorescence decay kinetics obtained for the EDFs M12 (a) and L110 (b). Curves 1 to 6 are captured for different pump levels (see the insets in the right upper corners). Zero-time corresponds to the moment when the pump light is switched off.

It is seen from Figure 11 that for these two EDFs fluorescence power, corresponding to 1.53-μm spectral band, is saturated (as is saturated GSA of Er^{3+} ions) yet at a few mW of pump power. However the key feature is deviation from the exponential law in the fluorescence kinetics in EDF L110 (see Figure 11(b)). A similar trend occurs but is less expressed in the rest of L and M fibers with lower Er^{3+} concentration; see e.g. Figure 11(a). Another fact deserving attention is the presence of a sharp drop in the fluorescence signal in fiber L110 at high pump powers, which happens after switching pump off (refer to curves 4–6 in Figure 11(b)). Such a feature is present but in a smaller degree also in fibers L40, L20, and M12 (having substantially lower Er^{3+} contents) and almost vanishes in fiber M5 (having the lowest Er^{3+} content). Note that similar fluorescence kinetics were observed in some of the earlier reports, see e.g. [4, 10].

http://dx.doi.org/10.5772/59146

Overview of the fluorescence decays for all the EDFs under scope is provided in Figure 12 (points). These data were obtained at maximal pump power, P_p at 978 nm (400 mW; the high pump power was found to be the right choice for minimizing spatial diffusion of excitation; see e.g. [10]). The dependences in the figure demonstrate the fluorescence decay "tails" obtained after cutting off the short initial segments just after switching pump off (~30 μs), which permits elimination of the influence of non-instant LD power decay (~8 μs).

As seen from Figure 12, 1.53-μm fluorescence decays get more and more deviated from the single exponential law when Er^{3+} concentration increases: The fibers with smaller contents of Er^{3+} ions (M5, M12, and L20) demonstrate decays nearly a single-exponent law whereas fibers L40 and L110 – the decays, apparently different from this law. These features, associated to the Er^{3+} concentration effect, can be addressed in terms of the IUC process – see Section 3.3 where the results of modeling of Er^{3+} fluorescence kinetics are presented. The modeling of the fluorescence kinetics allowed us to get, for each EDF, lifetime τ_0 and constant C_{HUP*} (characterizing the homogeneous UC process, HUC; see modeling below) and thereafter to build their dependences upon small-signal absorption value α_0 at 1.53 μm (and hereby upon Er^{3+} ions concentration, proportional to α_0).

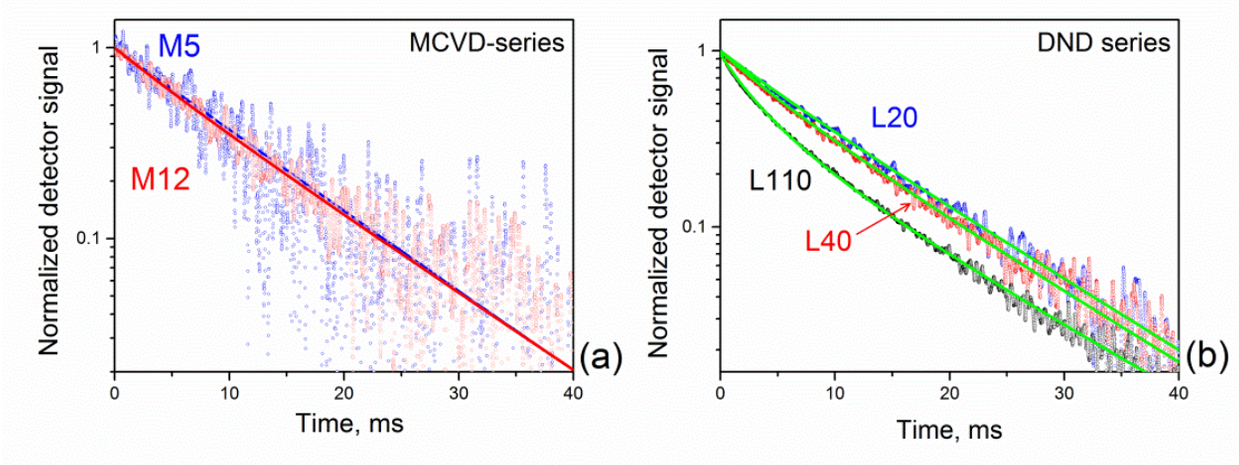

Figure 12. Normalized fluorescence decay kinetics obtained for the EDFs of L-(a) and M-(b) series; points – experimental data (using InGaAs-PD with Si filtering); plain curves are the theoretical fits made using formula (22).

Furthermore, Figure 13 demonstrates the results of the fluorescence kinetics' measurements in the optical band below 1.1 μm within a short (tens of μs) interval just after switching pump light off, for EDFs M12 (a), L40 (b), and L110 (c). The measurements were fulfilled using Si-PD without optical filtering at P_p=400 mW. As is seen from the figure, there are two "fast" components in the PD signal's decay: The shortest (≈8 μs) one, being in fact the setup's technical resolution and originating from the scattered pump light, and the longer one, measured by 21 μs to 26 μs for fibers M12, L40, and L110 (for fibers M5 and L20 this component was not resolved). A similar component was also detected in the 1.53-μm fluorescence kinetics; see Figure 11, which evidences its non-radiative nature. Note that there are known the processes in Er^{3+} -doped materials attributed by similar times [19, 20].

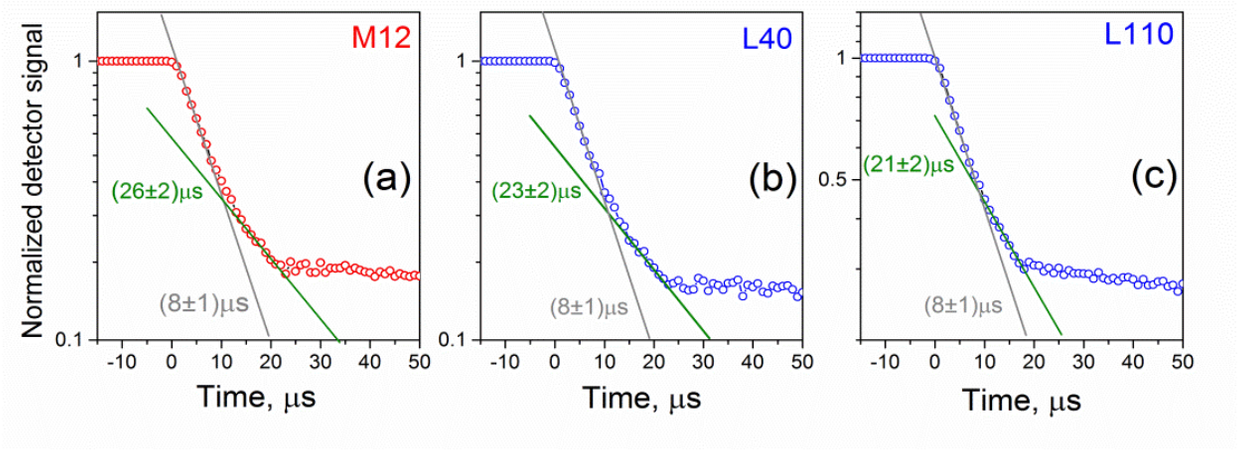

Figure 13. Fluorescence decay kinetics in the EDFs measured using Si-PD: M12 (a), L40 (b), and L110 (c); the short-time components of the fluorescence signals are specified in each plot.

We suggest that the found feature stems from a partial excitation relaxation in Er^{3+} clusters since it is present in the heavier doped EDFs but almost vanishes in the lower doped ones. The magnitude of the short-living component is a function of Er^{3+} concentration (and therefore of α_0), as seen when comparing the plots (a), (b), and (c) in Figure13: The higher Er^{3+} concentration the larger is relative (to the technical, i.e. originated from pump-light scattering) magnitude of this component.

3.3. Nonlinear absorption coefficient

The nonlinear absorption coefficient of a rare-earth doped fiber (e.g. EDF) as a function of pump power $\alpha(P_p)$ contains the useful information about GSA saturation and, consequently, about the fiber's potential as a laser medium. On the other hand, such effects deteriorating laser 'quality' of the fiber as ESA and concentration-related HUC / IUC (lifetime quenching and non-saturable absorption) ought to affect the behavior of $\alpha(P_p)$, too [18].

In the study to be reported hereafter, pump light was delivered to an EDF sample from the same LD operated at 978 nm (used in the measurements of fluorescence spectra and lifetimes); pump power was varied from ≈0.5 to 400 mW. We measured first the nonlinear transmission coefficient of the EDF sample with length L_0, which is defined as $T_{978}=P_P^{out}/P_P^{in}$ where P_P^{in} and P_P^{out} are the pump powers at the EDF's input and output. Then we made a formal re-calculation of the experimental transmission coefficient $T_{978}\left(P_P^{in}\right)$ in the absorption coefficient, applying formula: $\alpha\left(P_P^{in}\right)=-ln\left(T_{978}\right)/L_0$. The EDFs' lengths were chosen such that overall trends in the dependences $\alpha\left(P_p^{in}\right)$ can be viewed within the whole range of pump powers. The ratio of the EDFs' lengths was such that the optical density (the product $\alpha_0 L_0$) is almost the same for all the samples, which is worth for estimation of the nonlinearity (saturation) of absorption at increasing Er^{3+} concentration in the fibers. Using the OSA, we checked the ratio of pump to ASE powers at the EDFs' outputs; it was found that the ASE contribution is negligible in all samples at $P_p^{in}>0.5$ mW.

http://dx.doi.org/10.5772/59146

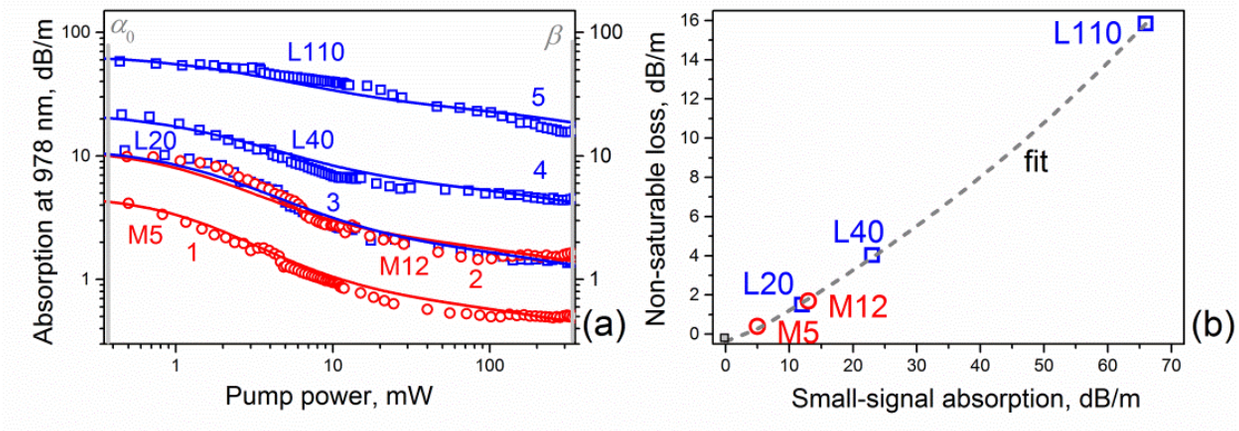

Figure 14. (a) Nonlinear absorption coefficients of the EDFs of L-and M-types vs. pump power at 978 nm. Symbols: experimental points; plain curves: theoretical fits obtained using Eqs. (25-27). Fiber lengths used in experiments and at modeling were, correspondingly: 188.6 (M5, curve 1), 59.4 (M12, curve 2), 43.5 (L20, curve 3), 22.4 (L40, curve 4), and 9.5 (L110, curve 5) cm. (b) Non-saturable absorption β vs. small signal absorption α_0, measured for the entire EDFs' set; the fitting curve is for guiding the eye.

The results obtained by applying the drawn procedure are shown in Figure 14(a) by symbols. Coefficients α_0 and β (saturated absorption at pump wavelength) marked in the upper left and right corners of the figure correspond to the limits of small-signal and saturated pump absorptions. First notice that absorption is "bleached" (in other words, transmission is "saturated") by a more or less similar manner for either fiber. However, as is also seen from the figure, the "residual" absorption (β) rises drastically with increasing Er^{3+} concentration in the fibers' sequences M5→M12 and L20→L40→L110. This trend points out that the ratio between the residual (β) and small-signal (α_0) absorptions is much bigger for the heavier doped fibers (M12, L40 and L110). In fact, pump-induced (looking as residual) absorption β is the measure of nonlinear absorption loss in EDF, as it stems from the modeling results (see Section 3.4 below). Furthermore, the dependence $\beta(\alpha_0)$ plotted in Figure 14(b) allows one to reveal that this pump-induced excessive loss in the EDFs appear as one of the most important Er^{3+} concentration effects.

3.4. Modeling

Firstly, the kinetics of near-IR (~1.53 μm) fluorescence decays obtained for the entire set of the EDF samples were modeled, which allows us to find Er^{3+} fluorescence lifetimes τ_0 and HUC coefficient C_{HUP}. The model implicitly implies, in accord to the definition of the HUC process, the only interactions between rather distant single Er^{3+} ions, not forming "chemical", tightly coupled, clusters, which are in turn supposed to interact via the IUC mechanism, discussed further. At this step of modeling we disregard the short-time features in the fluorescence decays, which are assumed to originate from Er^{3+} ions gathered into quenched (weakly fluorescing) clusters. That fact that in the experiments on fluorescence kinetics we used comparatively high pump powers (400 mW) allows us to neglect the intensity dependent HUC contribution and excitation migration effects.

For the normalized population density n_2^s of single (index "s") Er^{3+} ions being in the first excited (laser) state $^4I_{13/2}$, the following rate equation holds [21]:

$$\frac{dn_2^s}{dt} = -\frac{n_2^s}{\tau_0} - C_{HUP}\left(n_2^s\right)^2 \tag{21}$$

where $n_2^s = N_2^s / N_0^s$; N_0^s is the population density of single Er^{3+} ions in the excited state 2 ($^4I_{13/2}$), N_0^s is their concentration, and C_{HUP} [s^{-1}] is the UC parameter, being a product of the "volumetric" HUC constant C_{HUP}^* [$s^{-1}cm^3$] and concentration N_0^s: $C_{HUP} = N_0^s C_{HUP}^*$.

Assuming that pump power at 978 nm is high enough to achieve maximal populating of the excited state $^4I_{13/2}$, i.e. at "infinite" pump power, the part of Er^{3+} ions being in the excited state is $k=\sigma_{12}/(\sigma_{12}+\sigma_{21})$. Furthermore, since in our experimental circumstances (where near-IR fluorescence is detected at ~1.53 μm while excitation is at λ_p=978 nm) the SE process can be disregarded by means of formal zeroing cross-section σ_{21} in the dominator of this ratio (k=1). Implying that $n_2^s(t=0)=1$ and that pump is switched off at t=0, equation (21) is solved analytically, giving:

$$n_2^s(t) = \frac{e^{-\frac{t}{\tau_0}}}{1 + \tau_0 C_{HUP}\left(1 - e^{-\frac{t}{\tau_0}}\right)} \tag{22}$$

Formula (21) is a worthy approximation for fitting of the whole of experimental near-IR fluorescence decay kinetics, reported above for P_p ~400 mW (providing maximal population of manifold $^4I_{13/2}$). The modeling results obtained by using formula (22) are shown by plain curves in Figure 12 (the fitting procedure has been fulfilled until the residual sum R^2 exceeded 0.99) and are seen to be in good agreement with the experimental decay kinetics (points in the figure). The values of constants τ_0 (lifetime of single Er^{3+} ions, found to be ~10.8 ms for all the fibers under study), and C_{HUP} (an attribute of the HUC process, determined as the result of fitting) are plotted in Figure 15 in function of the small signal absorption α_0 at 978 nm.

As seen from Figure 15, the parameter C_{HUP} is proportional to Er^{3+} concentration (GSA α_0 at 978 nm). From this figure we found the value of HUC constant: C_{HUP}^*=2.7×10^{-18} $s^{-1}cm^3$. This value agrees well with the published data for EDFs of similar types; see e.g. Refs. [22-24]. Note that the quantity attributing the HUC phenomenon (C_{HUP}^* constant) should be proportional to the ESA cross-section (see e.g. [25]). As the latter does not depend on Er^{3+} concentration, C_{HUP}^* should be concentration-independent. Indeed, the dependence C_{HUP} vs. α_0 is seen from Figure 15 to be almost linear.

The next step in modeling is simulation of Er^{3+} clusters' contribution on the base of the experimental dependences of nonlinear absorption vs. pump power (see Figure 14(a)). A method to model nonlinear absorption of an EDF is based on the idea that ensemble of Er^{3+} ions in a fiber consists of two independent subsystems, assumed to be single ("s") and clustered

http://dx.doi.org/10.5772/59146

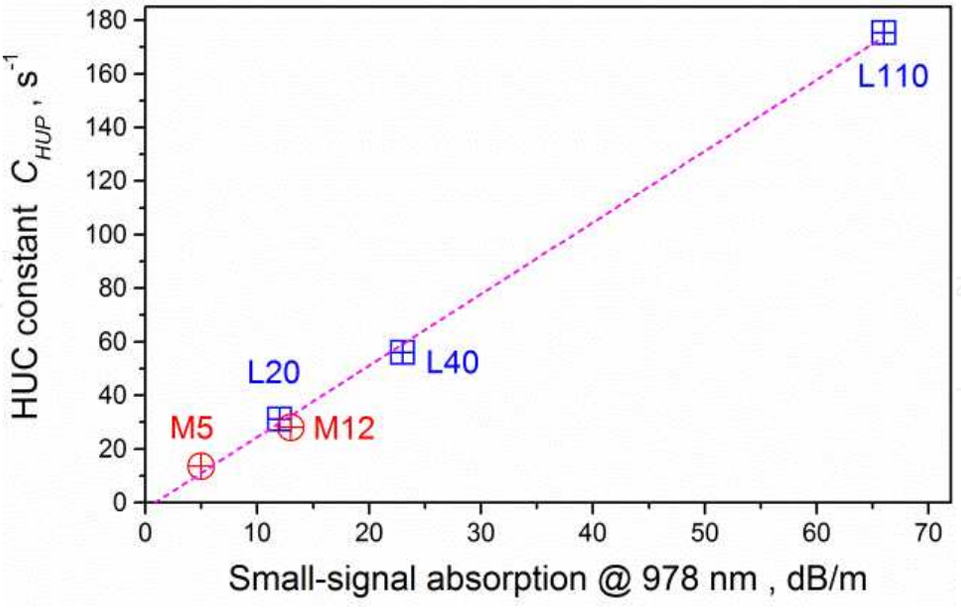

Figure 15. The values of HUC constant C_{HUP} vs. Er^{3+} concentration (in terms of α_0 at 978 nm), obtained for the entire set of EDFs as the result of modeling of the experimental fluorescence kinetic using formula (22); the fitting line in for guiding the eye.

("c") ions. Considering this hypothesis, we generalize the model developed in [21] for propagation of a pump wave through the system of single and paired resonantly absorbing and fluorescing centers (pairs are the simplest case of clusters). The model's generalization signifies here that the clusters' subsystem is meant to comprise an arbitrary number of centers (Er^{3+} ions in our case) whereas the other subsystem – to consist of single species [6, 26].

We assume that a cluster of Er^{3+} ions can occupy only one of the two permitted states – the state <11>, where all ions forming the cluster are in the ground state, and the state <12>, where one excepted ion (an acceptor of energy transferred from the adjacent donor ions within the cluster) is in the excited state. The latter holds because if other cluster's constituents absorb pump photons and move to the excited state, all them except one leave state 2 (down to state 1) immediately, whereas only this excepted one can stay in state 2.

We also take into account the presence of the short time τ_1 (together with much longer τ_0) for Er^{3+} clusters as an essential element of the model, coming from the experimental data.

We consider that the populations of single ($N_{1,2}^{S}$) and clustered ($N_{1,2}^{c}$) Er^{3+} ions, satisfy the following relations:

$$N_1^s + N_2^s = N_0^s = (1 - \chi\kappa)N_0 \tag{23}$$

$$N_1^c + N_2^c = N_0^c = \chi\kappa N_0 \tag{24}$$

where κ is the partial weight of clustered ions in ensemble, χ is the effective (averaged) number of Er^{3+} ions in a cluster, and N_0 is the total Er^{3+} ions concentration. The correspondent normalized population densities are defined as $n_{1,2}^{s,c} = N_{1,2}^{s,c} / N_0$, where the lower indices assign, correspondingly, the ground (1 or <11>) and the excited (2 or <12>) states, and $N_0^{s,c}$ are the concentrations of single ions and clusters, respectively.

The balance equations for pump power (P_p) and normalized dimensionless population densities of single and clustered ions being in metastable states 2 and <12>, $n_2^{s,c}$ ($0 \le n_2^{s,c} \le 1$), are as follows [27]:

$$\frac{dP_p(z)}{dz} = -\alpha_{p0}\left[1 - \left(1 + \xi_s - \varepsilon_s\right)\left(n_2^s(z) + n_2^c(z)\right)\right]P_p(z) - \alpha_{BG}P_p\left(z\right) \tag{25}$$

$$\frac{\alpha_0}{h\nu_p N_0 \Gamma_p A_c}\left[\chi\kappa - \left(1 + \xi_s\right)n_2^c(z)\right]P_p(z) - \left(\frac{1}{\tau_0} + \frac{1}{\tau_1}\right)n_2^c(z) = 0 \tag{26}$$

$$\frac{\alpha_{p0}}{h\nu_p N_0 \Gamma_p A_c}\left[1 - \chi\kappa - \left(1 + \xi_s\right)n_2^s(z)\right]P_p(z) - \frac{n_2^s}{\tau_0} - C_{HUP}\left(n_2^s\right)^2 = 0 \tag{27}$$

where majority of the quantities have been designated above, parameter $A_c = \pi a^2$ is the EDF core area (a=1.5 μm is the core radius), and α_{BG}=0.03...0.1 dB/m, depending weakly upon the EDF type). In formulas (25-27) we omit the ASE contribution as negligible in our experiments at pump powers exceeding 0.5 mW (see above). Note that these formulas are written in a general form, applicable not only to the Er^{3+} ion but also to any other resonantly absorbing center, having a three equivalent level system and subjected to the aforementioned concentration effects.

The modeling results are plotted by plain curves 1 to 5 in Figure 16(a). It is seen that they fit well the whole of the experimental data for the EDFs of both (M and L) types. Thus, the IUC process, treated by us as mostly non-radiative relaxation within Er^{3+} ion clusters, is justified as the key mechanism responsible for nonlinear absorption (attributed by coefficient β). The dependence of β upon Er^{3+} concentration in terms of small signal absorption α_{p0} is shown in Figure 16(b) (see curve 1) as the result of modeling; the errors' bars in the curve show uncertainties of fitting the experimental data by the theory.

When making the numerical calculations, we found that, once searching for the best fit of the experiment by the theory, any χ-value (χ=2, 3, and so on) can be used, with κ-value being varied accordingly. Thus, we have concluded that the product $\chi\kappa$ (a relative number of clustered Er^{3+} ions in the system) serves an adjusting parameter at fitting rather than quantities χ and κ separately. Given by the modeling results, useful insight can be made to interrelation between the relative number of clustered Er^{3+} ions $\chi\kappa$ (modeling: Figure 16(a)) and the measured nonlinear (saturated) absorption β (experiment: Figure 14(a)). Placing on the same plot (at double logarithmic scaling) the dependences of these two quantities vs. small-signal absorption α_{p0}, we found that they have the slopes related as (~1.44/~0.63) ≈ 2.3; see Figure 16(b). The found slope's value signifies the average number of Er^{3+} ions in clusters, whose

http://dx.doi.org/10.5772/59146

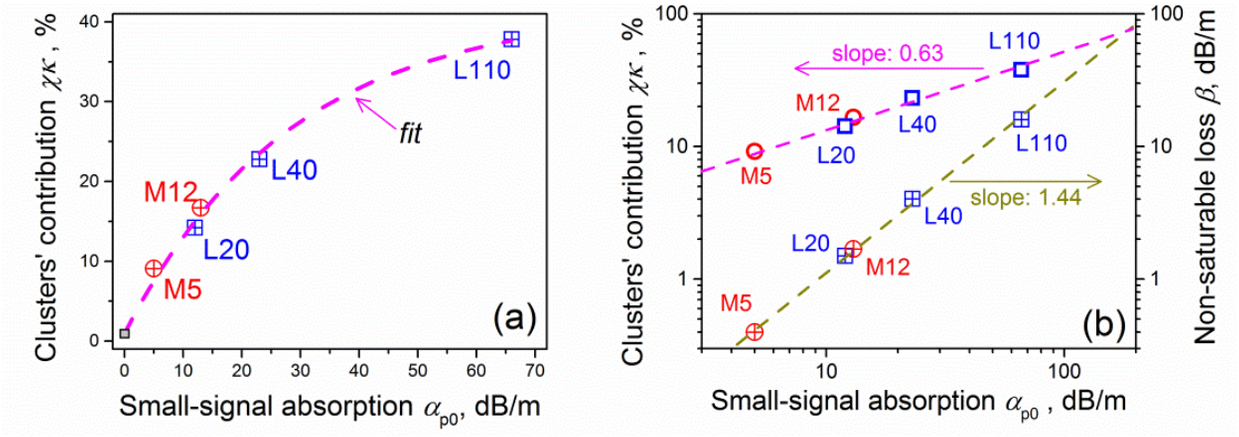

Figure 16. (a) Er^{3+} clusters' contribution $\chi\kappa$ vs. Er^{3+} concentration (in terms of α_{p0}) obtained for the entire set of EDFs of L-and M-types as the result of modeling the experimental dependences of nonlinear absorption coefficient using formulas (25-27); the fitting curve is for guiding the eye. (b) Er^{3+} clusters' contribution $\chi\kappa$ (left scale) and non-saturable absorption loss β (right scale) vs. Er^{3+} concentration (in terms of α_{p0}); the ratio of the slopes attributing the dependences reveals an effective number of Er^{3+} ions in clusters.

presence, according to the model, is responsible for NSA. This result deserves attention since it shows that NSA in the EDFs of both types mostly originates from paired Er^{3+} ions rather than from more complicate aggregates. Thus, in contrast to [28] where the role of "heavier" clusters in the IUC phenomenon is discussed, our results evidence for negligible contribution of Er^{3+} clusters, "heavier" than simple ion pairs.

Notice that the presence in EDFs of NSA at increasing Er^{3+} concentration affects net gain in heavily-doped Er^{3+} fibers, which becomes more and more limited (saturated) as it stems from the presence of single Er^{3+} ions being in the excited state, whereas the clustered ions, in their big part, i.e. ($\chi\kappa$–1) ions in each cluster, are always in the ground state. As a consequence, efficiency of an EDFL or EDFA is expected to drop down with increasing concentrations of Er^{3+} ions in the active fiber. Some recent studies confirm a severe character of the problem [29-30]. It seems that another problem could be encountered at the use of heavily-doped EDFs for pulsed operation where extensive heating via excitation relaxation within Er^{3+} clusters would affect the dispersive properties of the fibers and deteriorate the regime.

4. Effect of SBS upon operation of actively Q-switched EDFL

Actively Q-switched (AQS) EDFLs based on acousto-optics modulator (AOM), implemented in the Fabry-Perot geometry, usually produce Q-switch (QS) pulses with duration from a few to hundreds ns [1]. The QS pulses are normally composed of a few sub-pulses separated by round-trip time of photon inside the cavity [31, 32]; this AQS regime will be called further "conventional" (CQS). In the meantime, it is known that in certain conditions FLs demonstrate stochastic QS pulsing, which stems, as it will be clearly demonstrated below, from intra-cavity stimulated Brillouin scattering (SBS) [33]. Such pulses, referred further to as SBS-QS ones, are characterized by dramatic increasing of power as compared to CQS pulses but, at the same

time, by perceptible jitters [34]. In this section, we show that in certain circumstances SBS-QS pulsing is inherent in AOM-based AQS EDFLs. We also demonstrate that the areas (basins) where CQS and SBS-QS regimes exist are defined by definite values of EDF length and AOM's repetition rate and that the most important condition for turning of the laser to one or another pulsing regime is absence or presence of spurious narrow-line continuous wave (CW) lasing in the intervals where the laser cavity is blocked (AOM is switched OFF).

4.1. Experimental setup

An experimental setup of the QS-EDFL is sketched in Figure 17. The laser cavity consists of a piece of a standard low-doped "M" EDF (*Thorlabs*, M5-980-125), two FBGs (1 and 2) centered at ~1549.4 nm (laser wavelength), which form Fabry-Perot cavity, and a standard down-frequency shifting AOM with fiber outputs (*Gooch & Housego*, operation frequency – 111 MHz), placed nearby FBG2. The full AOM's rise time was measured to be 50 ns, AOM gate was fixed at 2 μs in experiments. FBGs' reflection coefficients were ~ 30% (FBG1) and ~ 100% (FBG2). A long period grating (LPG) tuned to ~1533 nm was used as in-line stop-band filter for neutralizing fiber gain at Er^{3+} SE peak and thus avoiding spurious CW lasing at this wavelength, which might otherwise discharge EDF and thereby reduce QS pulse energy and, via interfering with targeted pulsed lasing at the wavelength selected by FBGs, produce instability of pulsing. The EDF was pumped by a fiber-coupled 976-nm LD through a 980/1550-nm WDM. To decrease the cavity loss, FBG1 and LPG were written in the EDF core after preliminary hydrogenation. The laser signal was registered by OSA with a 50-pm resolution or by 1.2-GHz PD used in-line with a 2.5-GHz oscilloscope. In experiments, pump power was fixed at 500 mW and AOM's repetition rate (f_{AOM}) was varied within a 0...30-kHz range.

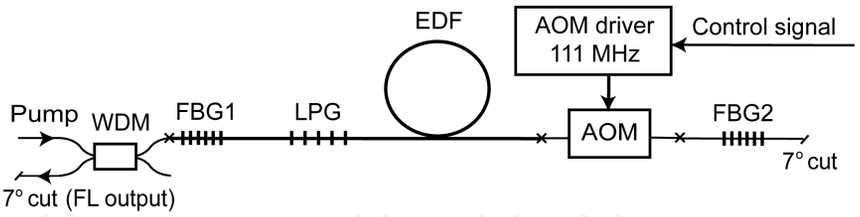

Figure 17. Experimental setup of the QS-EDFL (crosses indicate fiber splices).

4.2. Properties of CQS and SBS-QS regimes

As well-known, AQS FLs operated in CQS regime usually generate pulses consisting of train of sub-pulses (ripples), separated by a time interval equal to a photon's round-trip in the cavity. Such kind operation is fully described by the model of two contra-propagated waves in Fabry-Perot cavity, once considering the laser as a multi-pass amplifier of SE reflected several times by selective mirrors (FBGs) [32]. CQS is observed at any f_{AOM} when EDF length (L_{EDF}) is shorter than some specific value and at larger EDF when f_{AOM} is high. The common features of CQS pulsing observed experimentally and also modeled are as follows: Delay of a QS pulse with respect to the moment of AOM opening increases while its energy and power decrease with

http://dx.doi.org/10.5772/59146

increasing AOM's repetition rate. Usually, the first detectable sub-pulse arises in a few round-trips of ASE after AOM got opened. For example, when L_{EDF}=8.8 m and f_{AOM}=8 kHz, the first visible sub-pulse appears at ~250 ns (~2.5 photon round trips; see Figure 18(a)). The RF (FFT) spectrum of pulse train measured at f_{AOM}=16 kHz (see Figure 18(b)) has three peaks centered at 0 MHz, ~10 MHz and ~20 MHz. Width of peak 0 relates to QS pulses width, whereas peaks 1 and 2 correspond to the first and the second harmonics of the round-trip frequency (an inverted interval between sub-peaks, or round-trip time), respectively.

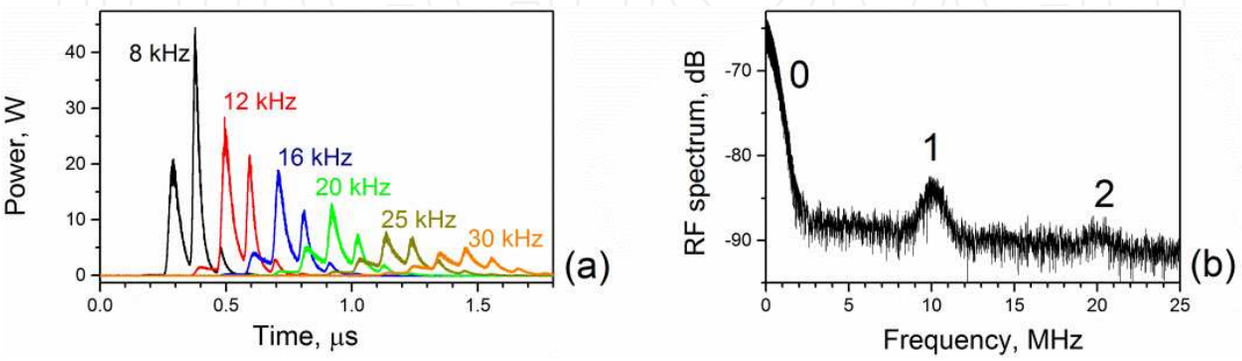

Figure 18. (a) CQS pulses registered on the EDFL output at L_{EDF}=8.8 m and at various f_{AOM}-values. Zero-time in both snapshots corresponds to the moment when AOM gets opened. (b) Averaged RF spectrum of CQS pulsing at f_{AOM}=16 kHz.

If the active fiber is long enough and AOM's repetition rate is not too high the QS EDFL turns into the regime of SBS-induced pulsing. This kind of pulsing is quite different as compared with CQS. Typical SBS-QS pulses are shown in Figure 19(a) for L_{EDF}=8.8 m and f_{AOM}=1 kHz. These pulses, as compared with CQS ones, arise earlier, approximately in ~180...280 ns after the moment of AOM's switching on; they are much narrower (~2.5...10 ns at 3-dB level); the pulses amplitude is more than by 10 dB higher as compared with the one at CQS while their envelop is apparently irregular. Emphasize that no SBS-QS pulses arisen within the intervals between the adjacent AOM's windows, in contrast to SBS-QS pulsing in an ytterbium-doped FL [34].

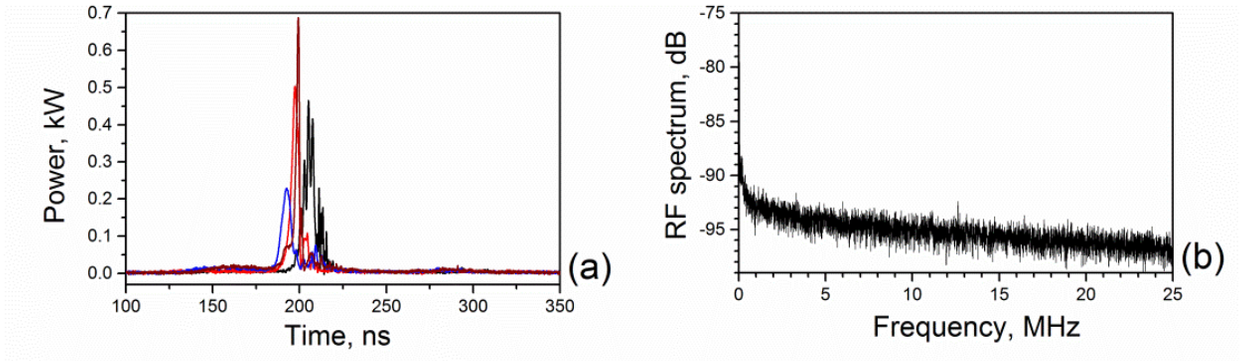

Figure 19. (a) CQS pulses registered on the EDFL output at L_{EDF}=8.8 m and f_{AOM}=1 kHz. (b) Averaged RF spectrum of CQS pulsing at f_{AOM}=1 kHz.

One more detail of SBS-QS is that pulses released in this regime suffer strong amplitude and timing jitters. Apparently, the presence of jittering is an indication of the stochastic nature of the SBS process involved. Furthermore, since the SBS-QS pulses are not composed of sub-pulses spaced by photon round-trip time, their RF (FFT) spectrum does not have peaks at the round-trip frequency (~10 MHz) and its harmonics (see Figure 19(b)).

4.3. Basins of CQS and SBS-QS regimes

To find basins of CQS and SBS-QS regimes existence, we measured the value of f_{AOM} at which the laser transits from one to another QS regime, for different L_{EDF}. The experimental points in the space (f_{AOM}, L_{EDF}) segregating CQS and SBS-QS operations were easily fixed since QS pulses captured at the laser output in these two regimes differ drastically in pulse amplitude, duration and shape (see snapshots in Figures 18(a) and 19(a)). We found that if L_{EDF} is less than or equal to a certain value (5.4 m in our arrangement) the laser operates in CQS regime, at any f_{AOM}. But if EDF is longer than 5.4 m, an operation regime depends on AOM's repetition rate: At low f_{AOM} the laser generates SBS-QS pulses while at high f_{AOM} it turns to CQS operation. The basins of CQS and SBS-QS regimes are illustrated in Figure 20. As seen from the figure, the laser operates in CQS and SBS-QS above and below the border line, respectively (this line schematically marks a transition between the regimes).

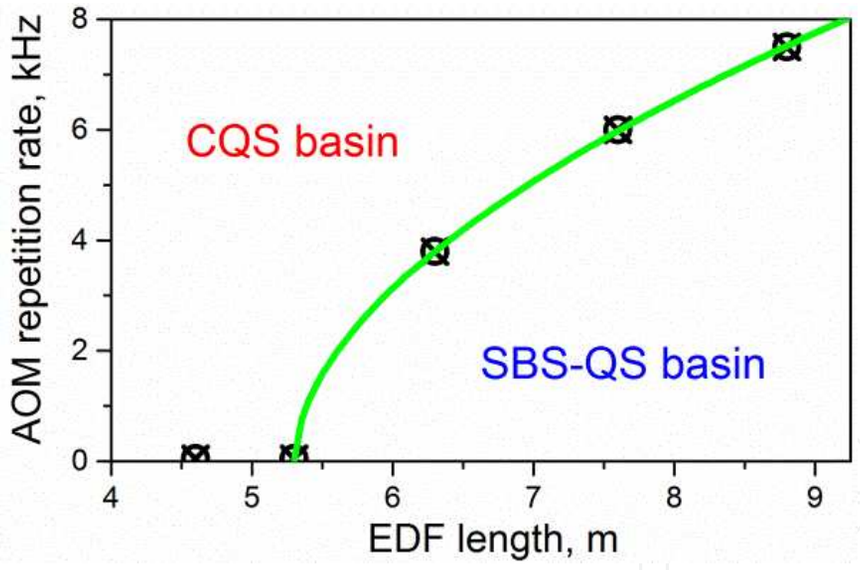

Figure 20. Basins of CQS and SBS-QS regimes; symbols label the experimental points corresponding to the border (solid line) between the basins.

The reason of the AQS-EDFL's switching to CQS or SBS-QS regime is the existence or the absence of spurious narrow-line CW lasing when AOM is blocked. In the last case the cavity is formed by the output reflector FBG1 and by a small reflection from closed AOM (~ –40 dB) ("bad" cavity). The overall loss of this cavity is estimated to be ~45-47 dB, revealing its very low Q-factor. At long EDF and low AOM repetition rates (the area below the border line in Figure 20) the EDF charge is sufficient to provide fiber gain capable of overcoming the cavity

http://dx.doi.org/10.5772/59146

loss, which results in arising CW lasing. After switching AOM on, the CW wave starts to propagate along the main laser cavity (formed by FBG1 and FBG2) with simultaneous amplification of its power by the EDF until the latter reaches SBS-threshold and produces a "giant" SBS-QS pulse. Thus, CW spurious lasing arising in the "bad" cavity is a startup mechanism for SBS-QS pulsing. In the area above the border line in Figure 20 the spurious CW lasing is not established since the EDF cannot accumulate gain sufficient to overcome the "bad" cavity's loss.

To confirm the hypothesis that the mechanism "igniting" SBS-QS pulsing relates to arising of the narrow-line CW lasing in "bad" cavity (when AOM is closed), we fulfilled the experiments on measuring the laser's optical spectra.

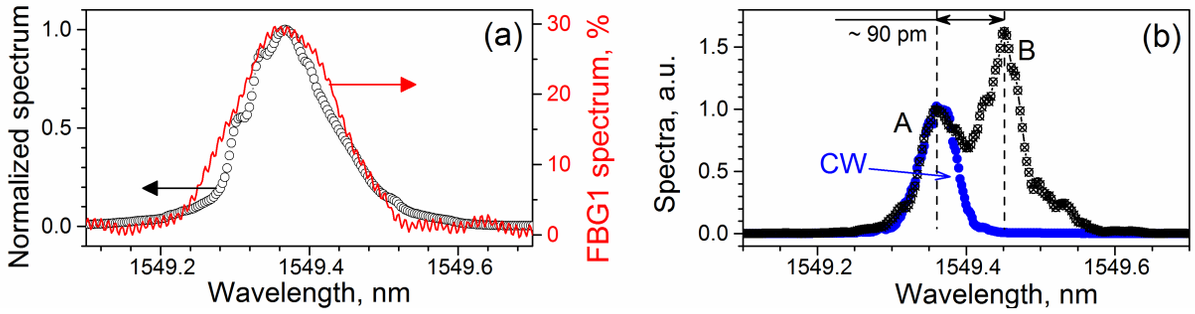

Figure 21. (a) Normalized AQS EDFL spectrum measured at f_{AOM}=8 kHz (open circles, left scale) and FBG1 spectrum (solid line, right scale). (b) Normalized AQS EDFL spectra measured at f_{AOM}=4 kHz (black crossed circles) and at AOM being always blocked (CW lasing, blue circles). In both cases L_{EDF}=7.6 m. OSA resolution is 50 pm.

Firstly, we compared the optical spectra of the laser operated in CQS and SBS-QS regimes; see Figure 21. Comparing the lasing spectra at f_{AOM}=8 kHz (CQS) and f_{AOM}=4 kHz (SBS-QS), one sees that in the former case (Figure 21(a)) the spectrum virtually repeats the reflection spectrum of FBG1 (the one of FBG2 is broader), whereas in the latter case (Figure 21(b)) it consists of two spectral lines A and B, spaced by ~90 pm (~11 GHz, a Brillouin shift at 1550 nm). Both laser lines A and B are narrower (~60 pm) than the lasing (in fact ASE) spectrum at CQS, ~160 pm. Supposedly, line A, centered at the FBG1's peak, corresponds to CW lasing arisen when AOM is in OFF state (between the adjacent AOM's gates) whereas line B – to SBS-QS pulsing. To provide more arguments in favor of this hypothesis, we plot in the same figure (Figure 21(b)) the spectrum of CW lasing, when the main cavity is always blocked (i.e. AOM is continuously in OFF state). It is seen that line A vastly reproduces the CW lasing spectrum. This allows us to reveal that the narrow line A is the signature of CW lasing and that it "ignites" the SBS-process; accordingly, the narrow line B, shifted by ~90 pm to the Stokes side, is the signature of SBS-lasing.

To shade more light on the scenario drawn above, we also measured the spectral width of spurious CW lasing arising when AOM is closed by employing another technique that utilizes a modified delayed self-heterodyne interferometer (DSHI, see Figure 22), described in details in [35-37]. To carry out this, the laser output signal was split into two beams, one of which being passed through an optical frequency shifter (AOM) and then through a long recirculating

fiber delay line made using SMF-28 fiber (L_d=20 km in our case). As the result, optical frequency was shifted by f_{AOM}=111 MHz at each pass along the delay line. After that, the signals (un-delayed and delayed) were combined and registered by a fast PD, connected to a RF spectrum analyzer (RFSA). To increase the method's sensitivity, an EDFA was included into the DSHI scheme at the fiber delay line's exit. We should note that the multi-pass self-heterodyne scheme used for estimation the EDFL's line width was chosen because, for correct measurements, the path difference should be much higher that the light source's coherence length (~ 20 km, see below).

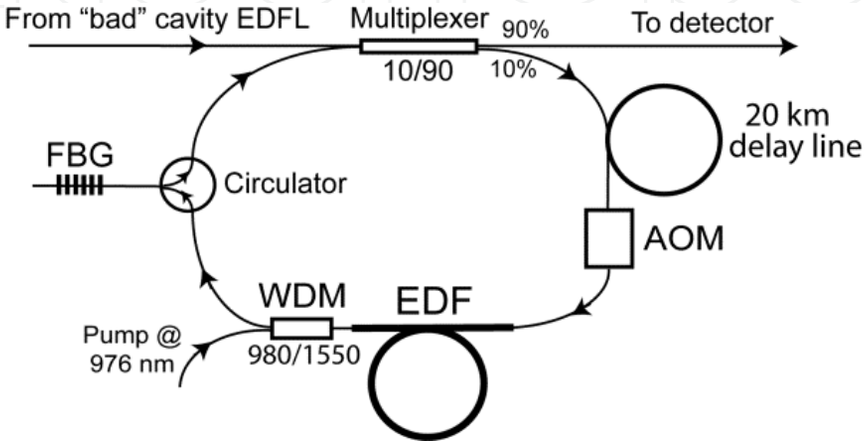

Figure 22. DSHI setup. AOM serves as a 111 MHz frequency shifter (always is open); 100%-FBG filters ASE produced by EDFA (reflects light only at the wavelength of the EDFL's "bad" cavity).

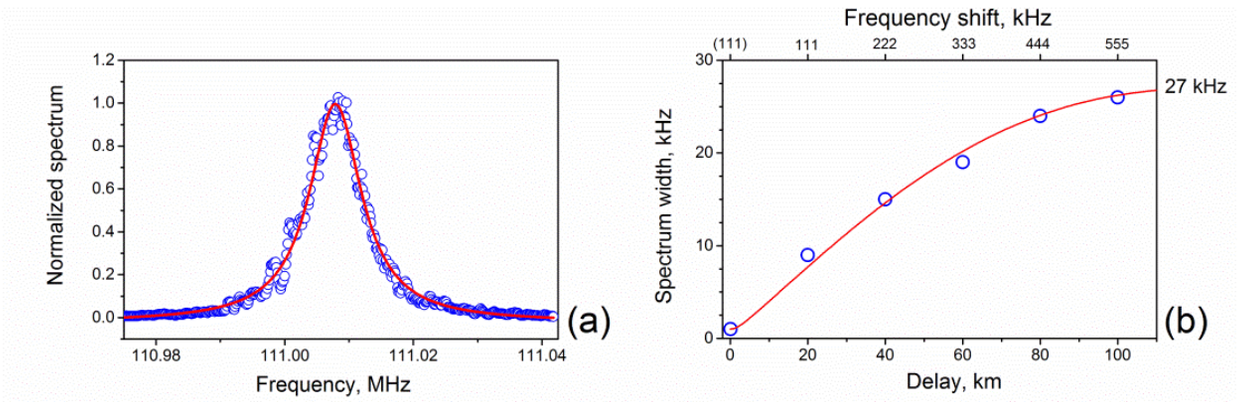

Figure 23. (a) An example of the CW EDFL RF-spectrum obtained from DSHI at 111 MHz; experimental data are shown by circles, solid line is a Lorentzian fit that gives 9.8-kHz width of the spectrum. (b) Spectrum width of CW EDFL measured using the DSHI technique at RF frequencies multiplied by AOM's frequency shift (111 MHz) when the cavity is blocked (circles). Solid line is a fit obtained using the theory presented in [37] (equation 16). The point at zero-delay was obtained with a 111-MHz frequency shift in the absence of delay line, which gives the RFSA's resolution (1 kHz).

Figure 23 shows the spectral width of the signals at the frequencies multiplied by the AOM's frequency shift, measured after fitting the DSHI signal by the Lorentzian law, in function of

the delay-line length $L_d \times N$ (N is the number of passes through the line). As shown in [35-37], at high N a signal's width approaches the real value of an EDFL's optical width; in our case, this value is ~30 kHz, which corresponds to coherence length of ~20 km. The earlier reports [38, 39] also revealed a very narrow EDFL's line.

Consequently, a narrow-line CW laser wave developing in "bad" cavity and being a prerequisite of SBS-QS pulsing is highly coherent. This explains why SBS is unavoidably boosted by spurious CW lasing in the "blocked" cavity after the moment of AOM's opening, when the EDF is strongly inverted and thus strongly amplifying. Indeed, "unlimited" in length and therefore "uniform" Brillouin dynamic grating [40], induced in intra-cavity EDF (the fiber is always shorter than the estimated coherence length, ~20 km), is the main cause of SBS-QS pulsing.

5. Conclusions

In this Chapter, we reported some of the important nonlinear-optic features of EDFs, which, on one hand, impact efficiency of CW EDFLs on their base and, on the other hand, underlie the operation regimes established in EDFLs Q-switched using AOMs.

In particular, we showed that strong ESA transitions inherent in the Er^{3+} system at both the pump (~978 nm) and the laser (~1550 nm) wavelengths and ions' clustering inherent in the EDFs heavily doped with Er^{3+} cause unavoidable nonlinear losses that, in turn, strongly reduce efficiency of EDFLs, as compared to efficiency of Ytterbium-doped fiber lasers. We demonstrated as well that for making a correct numerical modeling of an EDFL one needs to consider all kinds of the nonlinear losses intrinsic in EDFs.

We also discussed in details the peculiarities of EDFLs operated in actively Q-switched regime using AOM. We demonstrated that the operation regimes of these lasers strongly depend on EDF length and AOM's repetition frequency. Specifically, at short EDF length or at high AOM's repetition frequency the laser operates in "conventional" Q-switching regime (being in fact multi-pass amplification of Er^{3+} SE) where pulses with relatively moderate power and relatively long in duration are composed of several, stable in time, sub-pulses, separated by a photon's round-trip time in the cavity. Furthermore, if EDF length is long enough and AOM's repetition frequency is not too high, the laser turns to the completely different pulsing regime, characterized by much shorter and much powerful pulses; however, pulses of this type are subjected to noticeable timing and amplitude jitters, originated from the stochastic in nature SBS process, ignited by spurious narrow-line CW lasing in "bad" (at closed AOM) cavity.

Acknowledgements

Authors acknowledge support from the CONACyT, Mexico (Project No. 167945).

Author details

Y.O. Barmenkov* and A.V. Kir'yanov

*Address all correspondence to: yuri@cio.mx

Centro de Investigaciones en Optica, Leon, Guanajuato, Mexico

References

[1] Richardson D. J., Nilsson J., Clarkson W. A. High power fiber lasers: Current status and future perspectives [Invited]. Journal of the Optical Society of America B 2010;27(11): B63–92.

[2] Barmenkov Yu. O., Ortigosa-Blanch A., Diez A., Cruz J. L., Andres M. V. Time-domain fiber laser hydrogen sensor. Optics Letters 2004;29(21): 2461-3.

[3] Arellano-Sotelo H., Barmenkov Yu. O., Kir'yanov A. V. The use of erbium fiber laser relaxation frequency for sensing refractive index and solute concentration of aqueous solutions. Laser Physics Letters 2008;5(11): 825-9.

[4] Laming R. I., Poole S. B., Tarbox E. J. Pump excited-state absorption in erbium-doped fibers. Optics Letters 1988;13(12): 1084-6.

[5] Miniscalco W. J. Erbium-Doped Glasses for Fiber Amplifiers at 1500 nm. Journal of Lightwave Technology 1991;9(2): 234-50.

[6] Blixt P., Nilsson J., Carlinas T., Jaskorzynska B. Concentration-dependent upconversion in Er^{3+} -doped fiber amplifiers: Experiments and modeling. IEEE Transactions Photonics Technology Letters 1991;3(11): 996-8.

[7] Myslinski P., Chrostowski J., Koningstein J. A. K., Simpson J. R. Self-mode locking in a Q-switched erbium-doped fiber laser. Applied Optics 1993;32(3): 286-90.

[8] Escalante-Zarate L., Barmenkov Y. O., Cruz J. L., Andres M. V. Q-switch modulator as a pulse shaper in Q-switched fiber lasers. IEEE Photonics Technology Letters 2012;24(4): 312-4.

[9] Barmenkov Y. O., Kir'yanov A. V., Cruz J. L., Andres M. V. Dual-kind Q-switching of erbium fiber laser. Applied Physics Letters 2014;104(9): 091124.

[10] Nykolak G., Becker P. C., Shmulovich J., Wong Y. H., DiGiovanni D. J., Bruce A. J. Concentration-dependent $^4I_{13/2}$ lifetimes in Er^{3+} -doped fibers and Er^{3+} -doped planar waveguides. IEEE Photonics Technology Letters 1993;5(9): 1014-6.

[11] Guzman-Chavez A. D., Barmenkov Y. O., Kir'yanov A. V. Spectral dependence of the excited-state absorption of erbium in silica fiber within the 1.48–1.59 μm range, Applied Physics Letters 2008;92(19): 191111.

[12] Bellemare A. Continuous-wave silica-based erbium-doped fibre lasers. Progress in Quantum Electronics 2003;27(4): 211–66.

[13] Krug P. A., Sceats M. G., Atkins G. R., Guy S. C., Poole S. B. Intermediate excited-state absorption in erbium-doped fiber strongly pumped at 980 nm. Optics Letters 1991;16(24): 1976-8.

[14] Barnes, W. L. Laming, R. I. Tarbox, E. J.; Morkel, P. R. Absorption and emission cross-section of Er^{3+} doped silica fibers. IEEE Journal of Quantum Electronics 1991;27(4): 1004-10.

[15] Bolshtyansky M., Mandelbaum I., Pan F. Signal Excited-State Absorption in the L-Band EDFA: Simulation and Measurements. Journal of Lightwave Technology 2005;23(9): 2796-9.

[16] Barmenkov Y. O., Kir'yanov A. V., Guzman-Chavez A. D., Cruz J. L., Andres M. V. Excited-state absorption in erbium-doped silica fiber with simultaneous excitation at 977 and 1531 nm. Journal of Applied Physics 2009;106(8): 083108.

[17] del Valle-Hernandez J., Barmenkov Y. O., Kolpakov S. A., Cruz J. L., Andres M. V. A distributed model for continuous-wave erbium-doped fiber laser. Optics Communications 2011;284(22): 5342–7.

[18] Kir'yanov A. V., Barmenkov Y. O., Il'ichev N. N. Excited-state absorption and ion pairs as sources of nonlinear losses in heavily doped Erbium silica fiber and Erbium fiber laser. Optics Express 2005;13(21): 8498-507.

[19] Kik P. G., Polman A., Exciton–Erbium interactions in Si nanocrystal-doped SiO_2. Journal of Applied Physics 2000;88(4): 1992–8.

[20] Kik P. G., Brongersma M. L., Polman A. Strong exciton-Erbium coupling in Si nanocrystal-doped SiO_2, Applied Physics Letters 2000;76(17): 2325–7.

[21] Kir'yanov A. V., Dvoyrin V. V., Mashinsky V. M., Barmenkov Y. O., Dianov E. M. Nonsaturable absorption in alumino-silicate bismuth-doped fibers. Journal of Applied Physics 2011;109(2): 023113.

[22] Berkdemir C., Ozsoy S. On the temperature-dependent gain and noise figure of C-band high-concentration EDFAs with the effect of cooperative upconversion. Journal of Lightwave Technology 2009;27(9): 1122–7.

[23] Jung M., Chang Y. M., Jhon Y. M., Lee J. H., Combined effect of pump excited state absorption and pair-induced quenching on the gain and noise figure in bismuth oxide-based Er^{3+} -doped fiber amplifiers, Journal of the Optical Society of America B 2011;28(11): 2667–73.

[24] Valles J. A., Bordejo V., Rebolledo M. A., Diez A., Sanchez-Marin J. A., Andres M. V. Dynamic characterization of upconversion in highly Er-doped silica photonic crystal fibers. IEEE Journal of Quantum Electronics 2012;48(8), 1015–21.

[25] Hehlen M. P., Cockroft N. J., Gosnell T. R., Bruce A. L., Nikolak G., Shmulovich J. Uniform upconversion in high concentration Er^{3+} -doped soda lime silicate and aluminosilicate glasses. Optics Letters 1997;22(11): 772–4.

[26] Myslinski P., Nguyen D., Chrostowski L., Effects of concentration on the performance of Erbium-doped fiber amplifiers. Journal of Lightwave Technology 1997;15(1): 112–9.

[27] Kir'yanov A. V., Barmenkov Y. O., Sandoval-Romero G. E., Escalante-Zarate L. Er^{3+} Concentration effects in commercial erbium-doped silica fibers fabricated through the MCVD and DND technologies. IEEE Journal of Quantum Electronics 2013;49(6): 511-21.

[28] An H. L., Pun E. Y. B., Liu H. D., Lin X. Z. Effects of ion clusters on the performance of heavily doped Erbium-doped fiber laser. Optics Letters 1998;23(15): 1197–9.

[29] Lim E.-L., Alam S. U., Richardson D. J., High energy in-band pumped Erbium doped fibre amplifiers. Optics Express 2012;20(17): 18803–18.

[30] Lim E.-L., Alam S. U., Richardson D. J. Optimizing the pumping configuration for the power scaling of in-band pumped Erbium doped fiber amplifiers. Optics Express 2012;20(13), 13886–95.

[31] Lim E. L., Alam S. U., Richardson D. J. The multipeak phenomena and nonlinear effects in Q-switched fiber laser, " IEEE Photonics Technology Letters 2011;23(23): 1763–5.

[32] Kolpakov S. A., Barmenkov Y. O., Guzman-Chavez A. D., A. V. Kir'yanov, Cruz J. L., A. Diez, Andres M. V. Distributed model for actively Q-switched erbium-doped fiber lasers. IEEE Journal of Quantum Electronics 2011;47(7): 928–34.

[33] Fotiadi A. A., Megret P., Self-Q-switched Er-Brillouin fiber source with extra-cavity generation of a Raman supercontinuum in a dispersion shifted fiber. Optics Letters 2006;31(11), 1621–3.

[34] Barmenkov Y. O., Kir'yanov A. V., Andres M. V. Experimental study of the nonlinear dynamics of an actively Q-switched ytterbium doped fiber laser. IEEE Journal of Quantum Electronics 2012;48(11): 1484–93.

[35] Tsuchida H. Simple technique for improving the resolution of the delayed self-heterodyne method. Optics Letters 1990;15(11): 640–2.

[36] Dawson J. W., Park N., Vahala K. J., An improved delayed self-heterodyne interferometer for linewidth measurements. IEEE Photonics Technology Letters 1992;4(9): 1063–5.

[37] Horak P., Loh W. H. On the delayed self-heterodyne interferometric technique for determining the linewidth of fiber lasers. Optics Express 2006;14(9): 3923–8.

[38] Chernikov S. V., Taylor J. R., Kashyap R., Coupled-cavity erbium doped lasers incorporating fiber grating reflectors. Optics Letters 1993;18(23): 2023–5.

[39] Choi K. N., Taylor H. F. Spectrally stable Er-fiber laser for applications in phase-sensitive optical time-domain reflectometry. IEEE Photonics Technology Letters 2003;15(3): 386–8.

[40] Song K. Y. Operation of Brillouin dynamic grating in single-mode optical fibers. Optics Letters 2011;36(23): 4686–8.

IntechOpen